University of Alberta

Power Management of Power Electronics Interfaced Low-Voltage Microgrid in Islanding Operation

by

Yan Li

A thesis submitted to the Faculty of Graduate Studies and Research
in partial fulfillment of the requirements for the degree of

Master of Science
in
Power Engineering and Power Electronics

Department of Electrical and Computer Engineering

Spring 2010
Edmonton, Alberta

Examining Committee

Yunwei Li, Electrical and Computer Engineering

Venkata Dinavahi, Electrical and Computer Engineering

Amit Kumar, Mechanical Engineering

Abstract

Distributed generation systems based on renewable energy sources have been experiencing rapid development in recent years. As well, a more recent concept called microgrid is developed by grouping a cluster of loads and paralleled DG units in a common local area.

This thesis focuses on the power control of power electronics interfaced low-voltage microgrid in islanding operation. A novel frequency-voltage frame transformation is proposed to improve the system stability and offset the power coupling in a low-voltage grid. A control algorithm to guarantee that the microgrid can be operated within the predetermined voltage and frequency variation limits is also proposed. Moreover, an adaptive reactive power droop method is proposed, which automatically updates the maximum reactive power limit of a DG unit based on its current rating and actual real power output, and features an enlarged power output range and improved system stability. Both simulation and experimental verification results are provided.

Acknowledgements

I would like to express my gratitude to all the persons who gave the help and support to complete this research work and thesis.

I am deeply indebted to my supervisor, Dr. Yunwei Li, for the continuous support of my M.Sc study and research, for his patience, enthusiasm, and immense knowledge. His guidance helped me in all the time of research and writing of this thesis.

I also would like to give my thanks to the colleagues from the Power Lab, who helped and supported me in the research work. Especially, I want to thank Mr. ChingNan Kao’s help in the experiment part.

Last but not the least, I would like to thank my family: my parents (Longsheng Li and Shuying Wu), my husband (Chuxiong Miao), and my daughter (Rachel W Miao), for their understanding and support, whose patient love enabled me to complete the research work.

Contents

List of Figures

List of Tables

Chapter 1

Introduction

This chapter starts with an overview of the distributed generation (DG), renewable energy sources (RES) and microgrid and provides the background information for the work in this thesis. Next, the challenges related to microgrid operation are discussed. Finally, this thesis' research objectives and research approach are described.

1.1 Distributed Generation

Distributed generation (DG) is the term used to describe small-scale power generation, usually in sizes ranging from a few kW to a few MW, located at a distribution system close to the loads [2]. In recent years, DG based on renewable energy sources (RES) and micro-sources have been experiencing rapid development due to their promising advantages in reducing air pollution, improving power system efficiency, and relieving the stress on power transmission and delivery systems [3].

Currently, most countries still generate most of their electricity in large central power plants. Due to a number of economic, safety, logistical, environmental, geographical and geological factors, these plants are usually built far away from the consumers. The generated power is then transmitted to the load centers over long transmission lines and distributed to the end customers over distribution systems. The drawbacks of this kind of power generation and transmission can be generally divided into two categories: problems relating to generation and ones relating to transmission.

The three major types of central power generation plants are (i) thermal plants using fuels such as coal, oil and gas; (ii) hydro plants; and (iii) nuclear power plants. For the traditional power generation plants, environmental issues are major problems. These plants are the major emitters of greenhouse gases, which are the main contributors to global warming. For the nuclear power plants, ensuring the safety of radioactive waste is a significant challenge and still unresolved problem. Furthermore, these plants' consumption of non-renewable energy to produce electricity may cause an energy shortage in the future. The hydroelectric plants are friendly to the environment, but have to be built near a place with sufficient water-flow due to their natural limits [1][4].

The main problems related to power transmission over long transmission lines include real power losses, reactive power consumption, and the systems' stability and reliability.

To overcome these problems and to focus on environment issues, researchers have made DG the main trend in electricity generation. They believe that the traditional system of large central power stations connected to their customers by hundreds or thousands of miles of transmission lines will likely be supplemented with cleaner, smaller plants located closer to their loads [2]. Using such DG systems can not only reduce transmission line losses and costs, but also has the potential to capture and utilize waste heat on-site through co-generation or combined heat and power generation (CHP), which greatly increases DG systems' overall efficiency and economic advantages. Moreover, DG systems can offer increased reliability and reduced threat of massive and widespread power failures, such as the blackouts that happened in various countries in recent years.

1.2 Renewable Energy Sources

One of the most important advantages of DG is that it can effectively use distributed RES, which are difficult for traditional large-scale and central power generation plants to use. Besides helping to relieve a possible worldwide energy shortage in the future, these RES-based DG systems can also help to address the environmental concerns associated with traditional power generation. For this reason, this section briefly reviews the main renewable electrical energy systems, such as wind power systems, PV power systems, and fuel cell systems.

1.2.1 Wind Power Systems

Wind energy is plentiful, renewable, widely distributed, and clean. The first wind-electric systems were built in the United States in the late 1890's, and wind turbine technology was developed continuously and rapidly, especially in Denmark, Germany, and Spain [2][4]. Figure 1.1 shows that the global installed capacity of wind turbines has been growing at over 30% per year since 2000 [5]. Based on a survey among the World Wind Energy Association (WWEA) member associations, the forecast for the

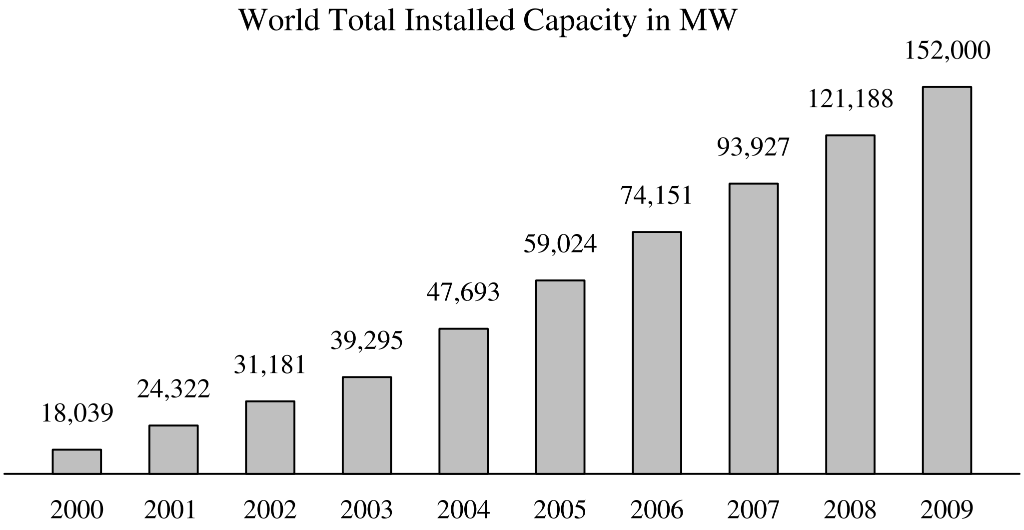

Figure 1.1: Worldwide installed wind-power capacity [a]

---

[a] From[5].

worldwide wind installation in 2009 was 152000 MW, which indicates a double digit growth for the wind energy market despite the general economic crisis [5].

1.2.2 Solar and PV Power Systems

Solar energy is energy obtained directly from the sun. PV is a technology that converts light directly into electricity. PV production has been doubling every two years, increasing by an average of 48% each year since 2002 [2], and is the fastest-growing energy technology in the world. PV is best known as a method for generating solar power by using solar cells packaged in PV modules, often electrically connected in multiples as solar PV strings and arrays to convert energy from the sun into electricity. Solar cells produce DC voltage from light, which can be used to power equipment or to recharge a battery. The first practical application of PV was to

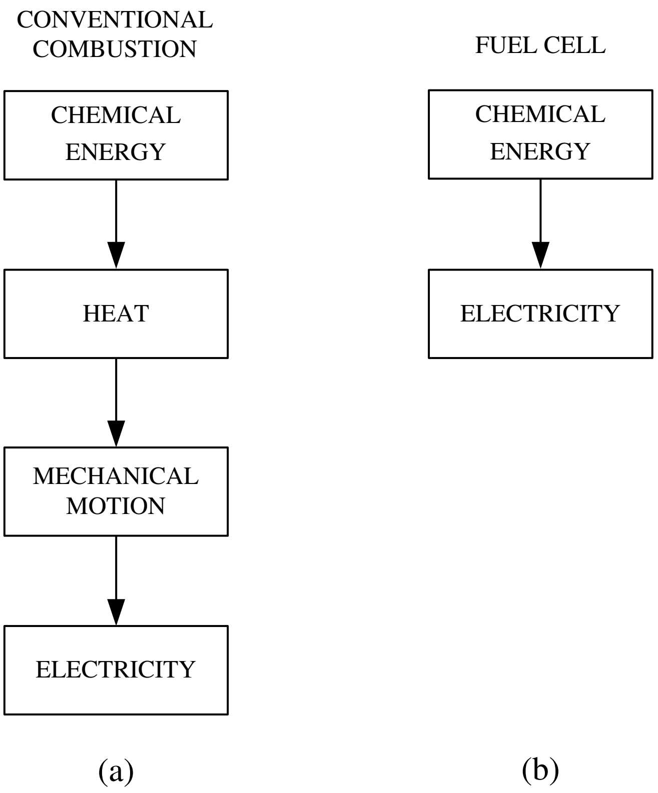

Figure 1.2: Energy conversion processes of (a) conventional combustion, (b) fuel cell

power orbiting satellites and other spacecraft and pocket calculators, but today the majority of PV modules are used for grid-connected power generation [2][6].

1.2.3 Fuel Cells

A fuel cell is an electrochemical energy conversion device. It produces electrical power directly from the chemical energy contained in a fuel (hydrogen, natural gas, methanol, etc). Unlike the conventional combustion power generation, which requires an intermediate step of converting fuel energy first into heat, which is then used to create mechanical motion and, finally, electrical power, as shown in Figure 1.2 (a), fuel cells transfer the chemical energy to electricity directly, as shown in Figure 1.2

(b). The fuel-to-electric-power efficiency for a fuel cell can be as high as 65%. This high efficiency gives fuel cells the potential to be roughly twice as efficient as the average central power station operating today [2].

Table 1.1: Distributed generation capabilities and system interfaces[1].

Technology	Typical Capability Ranges	Utility Interface
Wind	A few hundred W to a few MW	AC-DC-AC converter
Solar and PV	A few W to several hundred kW	DC-AC converter
Fuel Cell	A few tens of kW to a few tens of MW	DC-AC converter

To better describe the range of capabilities for the various technologies generally falling under the DG category, some typical DG capabilities and system interfaces are shown in Table 1.1 [1].

1.3 Power Electronics Interfaces

Despite the many advantages of RES-based DG systems, DG presents a quite different and challenging picture in terms of grid connection. For example, the voltage generated by variable speed wind-power generators (with variable output frequency), PV systems (DC voltage) and fuel cell systems (DC voltage) cannot be directly connected to a grid.

For the integration of RES-based DG systems into a utility grid, power electronic technology plays a key role not only in transforming the DC voltage or variable frequency AC voltage into voltage with the desired magnitude and frequency for a grid connection, but also in serving as a conditioning system to address the difference

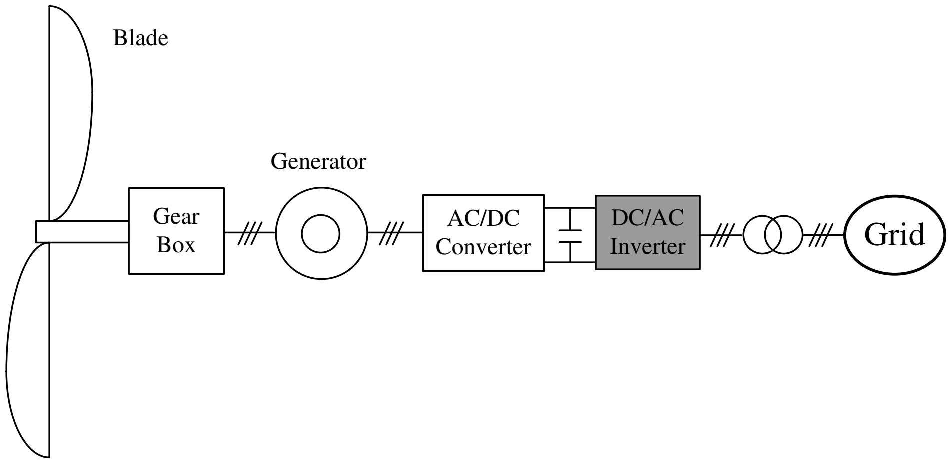

Figure 1.3: Wind turbine generator system with power electronics drive

between the DG units and the system and load requirements. With more and more DG units being integrated into power systems, power electronic technology is being widely used and rapidly expanding [7][8].

In the past few years, power electronics has rapidly evolved due to two main factors: (i) the development of fast semiconductor switches capable of switching quickly and handling high powers, and (ii) the development of digital controllers that can implement advanced and complex control algorithms. These factors have led to the development of cost-effective and grid-friendly converters [3][9][10].

The typical electronic interfaces used for different energy resources are shown in Figures 1.3-1.5.

Figure 1.3 shows the wind turbine generator system integrated into the grid by using power electronics as a drive system. In a wind power-generation system, the blades convert kinetic energy in the wind into rotating shaft power to spin a generator producing electric power. Variable-frequency AC voltage from the generator is rectified and converted into DC voltage by using an AC-DC converter. This DC

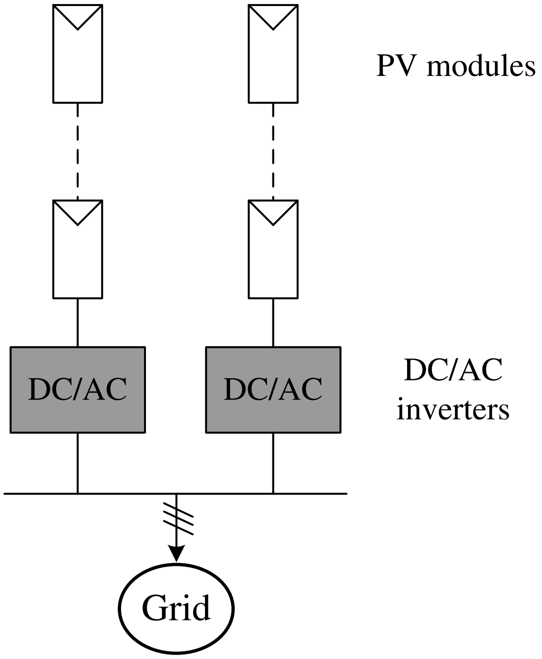

Figure 1.4: PV system with PV string converters

voltage is then sent to a DC-AC inverter that converts it back to AC voltage with the desired frequency and magnitude to make the AC voltage ready for grid connection.

Figure 1.4 shows a PV system with converters on each string. This configuration is commonly used today. Compared to a centralized inverter for an entire PV panel, the string converter system can have maximum power point tracking (MPPT) on each string. With roughly 15 PV modules in series, the DC voltage output of each string can be high enough to avoid voltage amplification, and therefore a DC-DC boost converter can be avoided (especially in North America where the residential voltage is 120V) [2].

Figure 1.5 shows a power electronic conditioning unit for fuel cell systems. In this example, a two-stage conversion including a DC-DC converter and a DC-AC inverter are shown, where the DC-DC converter is used for voltage isolation and

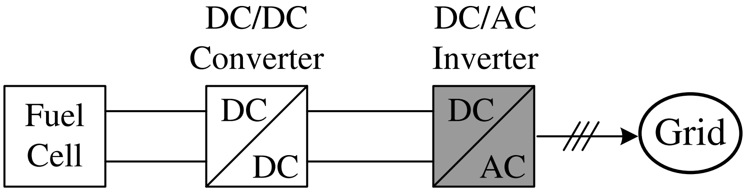

Figure 1.5: Fuel Cell power electronic conditioning system

voltage step-up, and the inverter is needed for generating the output AC voltage to meet the grid connection requirements. Similarly, if the fuel cell stack output voltage is sufficient, only a single DC-AC inverter is needed [11].

As Figures 1.3-1.5 reveal, a common feature of these power electronics interfacing systems is the grid side DC-AC inverter. This grid-connected inverter is the key component in such a DG system for generating output power that matches the grid voltage and meets the power-quality requirements. The research in this thesis is focused on the control of this grid-interfacing inverter.

1.4 Microgrid

Despite the increased penetration of DG systems, the application of individual DG systems always has its limitations such as high cost/W, limited capacity and reliability, and safety concerns. A better way to realize the emerging potential of DG is to take a system approach, which views generation and associated loads as a subsystem or a "microgrid." The microgrid is formed by grouping a cluster of loads and paralleled DG units in a common local area [12][13]. This approach allows for local control of DG, thereby enabling the systematic organization of DG system operations. Compared to a single DG, a microgrid has more capacity and control flexibility to fulfill

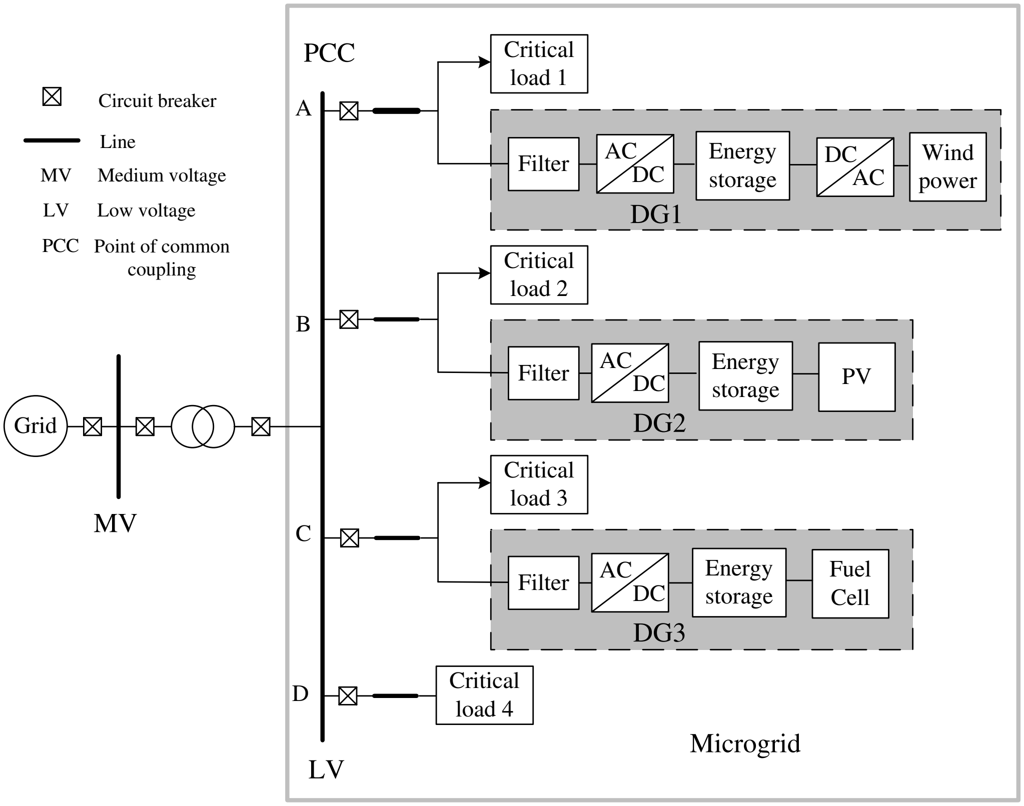

Figure 1.6: Microgrid configuration

system-reliability and power-quality requirements. A microgrid can therefore "behave well" and address the problems caused by single DG units. Furthermore, a microgrid can operate in either the grid-connected mode or the autonomous islanding mode and benefits both utilities and customers in terms of efficiency, reliability, and power quality [14][15].

1.4.1 Microgrid Configuration

Figure 1.6 shows an example of a microgrid configuration. In this example, the microgrid is assumed to be radial with four feeders, A, B, C and D. The radial microgrid system is often deployed as a small-scale distribution network at a low-voltage level. Three DG systems are in the microgrid. Each DG system has an energy source together with an energy-storage system, a power electronics interface, and output filters (LC filters or LCL filters).

A microgrid has two operation modes: the grid-connected mode and the islanding mode. In the grid-connected operation mode, the microgrid is connected to the main grid at the point of common coupling (PCC) through a circuit breaker, usually a static transfer switch (STS). In this mode, the DG systems are controlled to provide local power and voltage support for critical loads 1-4, and each DG unit generates the appropriate amount of real and reactive power according to the dispatched references or from the maximum power point tracking (MPPT). The excessive power generated in the microgrid can also be sent to the utility grid. As a result, the burden of power generation and transmission in the utility grid can be shared, and losses in the transmission lines can be reduced.

In case of a utility fault or power-quality event, the static switch can instantaneously separate the microgrid from the utility, and the microgrid will operate in the islanding mode. In the intentional islanding operation, the DG units continue to supply power to the loads in a microgrid and provide the uninterruptible power supply (UPS) function. In this operation mode, the DG systems in the microgrid are the only power sources to supply uninterrupted power to all the critical loads within the microgrid, and the DG units should be able to share the power demand in the microgrid automatically. When the fault in the utility is cleared and the microgrid is ready to be reconnected to the utility, a synchronization scheme is required to make sure the voltage at the microgrid terminal matches the utility voltage before the switch can be closed [12][16].

The proper operation of a microgrid requires the implementation of high-performance power-flow control and voltage regulation for each DG unit. The control method prefers to use variable control locally available to each DG unit, so that communication between DG units can be avoided. Doing so will improve the system reliability, reduce the system complexity, and reduce the costs. Moreover, with the communicationless feature, the “plug and play” [17] concept for each DG can be realized, so that a new DG unit can be connected to the system without affecting the operation of other DG units [12][18].

1.4.2 Low-Voltage Microgrid

Conventionally, modern electric power systems vary in their size and structural components, but they all have the same basic elements. Electric power is generated at a generating station and transmitted to consumers through a complex network. The transmission network is divided into mainly a transmission system and a distribution system.

Figure 1.7 shows the hierarchical structure of four levels of a power system network [19]. The transmission system interconnects all major generating stations and main load centres in the system. It forms the backbone of the integrated power system, of which the operating voltage level is typically 230 kV and above. The distribution system is the final stage in the system transfering electric power to the individual customers. The voltage level of distribution systems is typically less than 50 kV [20].

In such a power system, the RES-based inverter interfaced microgrid will be lo-

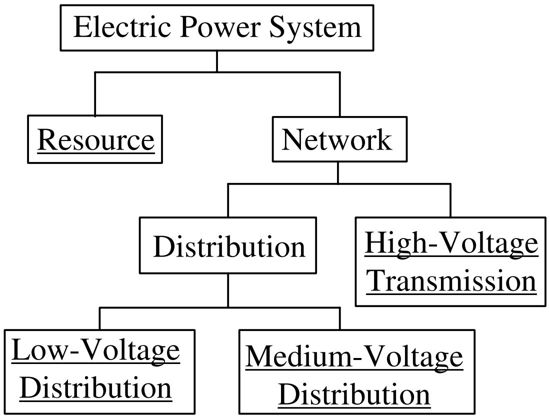

Figure 1.7: Hierarchy of power system network

cated at the low-voltage distribution network. More specifically, most power electronics interfaced DG units (except the large-capacity wind farms, which are connected to the transmission system) are connected to a network of voltages typically lower than 600V. For this reason, some important technical characteristics of a low-voltage distribution network are reviewed here [21].

- Structure. The majority of low-voltage distribution networks have a radial layout, and a number of low-voltage feeders are with the networks, starting from the low-voltage busbars of the infeeding medium voltage to the low-voltage substation. Every feeder may include one or more branches, and consumers are connected anywhere along the feeder or its branches.

- Symmetry. The connected consumers are normally single-phase, so that low-voltage networks are inherently unbalanced. Moreover, single-phase lines may exist, especially as feeder branches.

- Substation. The medium-voltage to low-voltage substation feeding the low-voltage distributed network normally includes a single transformer with a rating of a few hundred kVA up to 1 MVA. The transformer is equipped with off-load taps at the high-voltage winding, providing a typical regulation range of 5% [21]. Its connection group is usually Dyn 11, where the primary winding is Δ-connected, and the secondary winding is Y-connected. Thus, most low-voltage distributed networks are three-phase-four-wire systems.

- Protection. The only protection method for low-voltage networks is made up of simple phase over-current devices such as fuses. A medium-voltage to low-voltage transformer is protected by fuse links at the medium-voltage side, so no general protection element is present at the output of the transformer low-voltage winding, while every low-voltage feeder is protected by its own fuses. Typically, no other protection methods are used along the feeder or its branches.
- Line types. Both overhead lines and underground cables are popular for a low-voltage network. Overhead lines are used mainly for long distances in rural areas with a comparatively low load density. Aluminum and copper are the most common conductor metals for overhead lines. Underground cables are usually used in urban areas with a high load density or for underwater crossings. Generally, the cables have higher shunt capacitance and lower series inductance, as they are usually tightly spaced. In low-voltage systems, both overhead lines and underground cables have higher resistance compared to those in transmission systems.

The above discussion reveals that the low-voltage distribution system is a three-phase four-wire system or single-phase system with a radial structure. It has a very simple over-current protection system and is subject to unbalanced loading conditions.

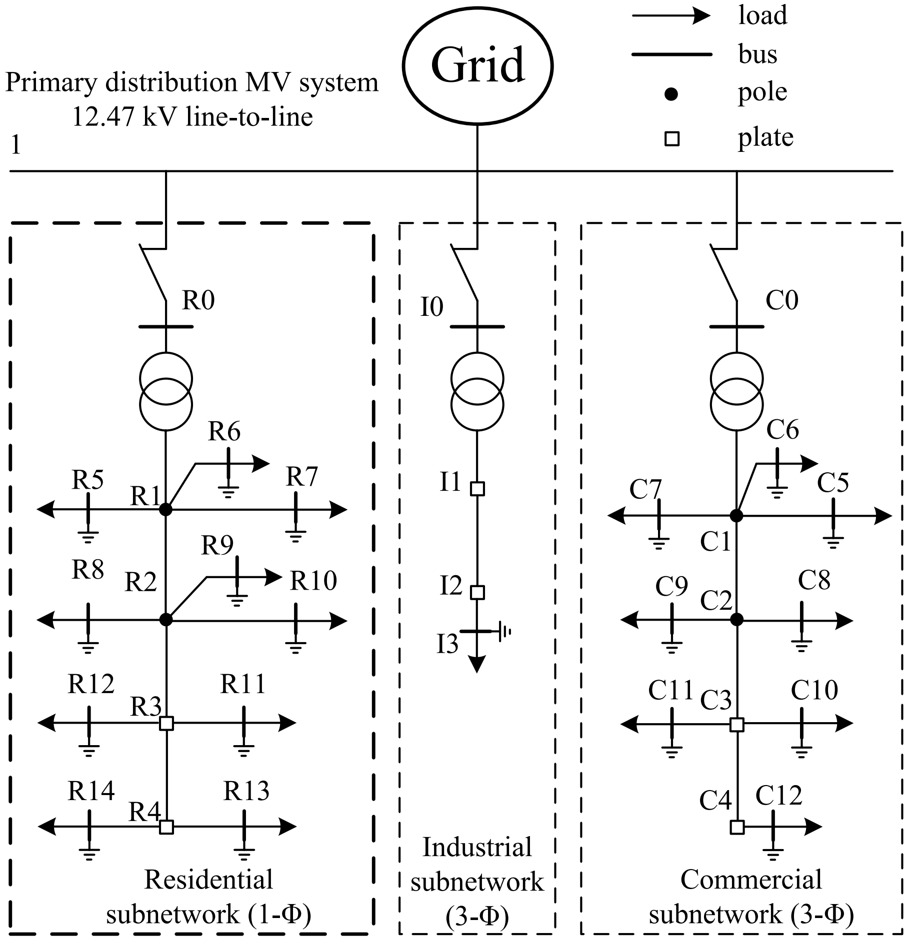

Figure 1.8: Topology of an example of a North American low-voltage distribution network

These features indicate that the control and protection of a DG system in such a low-voltage distribution network is challenging. Furthermore, unlike the transmission system, the feeder impedance of a low-voltage network is mainly resistive with a high R/X ratio, so that a mature control strategy in the transmission system cannot be directly used for a DG in a low-voltage distribution system.

Figure 1.8 shows the topology of an example of a North American low-voltage distribution network [19]. This distribution network is composed of three subsystems: a single-phase residential subsystem, a three-phase light industrial subsystem, and a three-phase light commercial subsystem. The parameters of the distribution feeders are given in Table 1.2, where R'_{ph} is the positive sequence resistance, and X'_{ph} is the positive sequence reactance. R'_0 and X'_0 are the zero sequence resistance and reactance, respectively, which are estimated by multiplying the positive sequence counterparts with an empirical factor of 1.6 [22]. The parameters of the subsystem distribution transformers are provided in 1.3 [19], where V_1 is the voltage of primary side and V_2 is the voltage of secondary side, LN stands for line to neutral and LL stands for line to line.

The line impedance is composed mainly of components R and L. For a transmission line in a high-voltage network with a large power-handling capability, R is small enough to reduce the power losses, and a high-voltage network has numerous generators and transformers. As a result the impedance representing the transmission line, generators, and transformers in a high-voltage network is mainly inductive. Based on the parameters in Table 1.2, the R/X ratios of the distribution feeders (including the overhead lines and the underground cables) in such a low-voltage distribution system range from 1.5 to 4. Obviously the feeder impedance in a low-voltage network is mainly resistive, and differs from the one in a high-voltage network.

In a low-voltage microgrid, the operation is further complicated by the large variation in the electrical distances between the DG units even within a small geographical area. For example, for direct coupled DG units, the impedance between two DG units is just the low-voltage distribution feeder, which has very small inductance and a high R/X ratio. In contrast, in case of DG units with LCL output filters

Table 1.2: Line parameters for low-voltage network

Node from	Node to	Types of lines	R'_{ph} (Ω/km)	X'_{ph} (Ω/km)	R'_{ph}/X'_{ph}	R'_0 (Ω/km)	X'_0 (Ω/km)	Length (m)
R1	R2	OH[1]	0.1509	0.0944	1.59851	N/A	N/A	25
R2	R3	UG[2]	0.1827	0.0711	2.56962	N/A	N/A	25
R3	R4	UG	0.1827	0.0711	2.56962	N/A	N/A	25
R1	R5	OH	0.3018	0.1265	2.38577	N/A	N/A	25
R1	R6	OH	0.6056	0.1503	4.02928	N/A	N/A	25
R1	R7	OH	0.3018	0.1265	2.38577	N/A	N/A	50
R2	R8	OH	0.3018	0.1265	2.38577	N/A	N/A	25
R2	R9	OH	0.3018	0.1265	2.38577	N/A	N/A	25
R2	R10	OH	0.6056	0.1503	4.02928	N/A	N/A	25
R3	R11	UG	0.1827	0.0711	2.56962	N/A	N/A	17
R3	R12	UG	0.3018	0.1265	2.38577	N/A	N/A	25
R4	R13	UG	0.3018	0.1265	2.38577	N/A	N/A	17
R4	R14	UG	0.3018	0.1265	2.38577	N/A	N/A	25
I1	I2	UG	0.1188	0.0798	1.48872	0.1901	0.1277	33
I2	I3	UG	0.1827	0.0798	2.28947	0.2923	0.1277	8
C1	C2	OH	0.1509	0.1032	1.46221	0.2414	0.1651	25
C2	C3	UG	0.1887	0.0798	2.36466	0.3019	0.1277	25
C3	C4	UG	0.1827	0.0798	2.28947	0.2923	0.1277	17
C1	C5	OH	0.3018	0.1352	2.23225	0.4823	0.2163	25
C1	C6	OH	0.3018	0.1352	2.23225	0.4823	0.2163	25
C1	C7	OH	0.3018	0.1352	2.23225	0.4823	0.2163	25
C2	C8	OH	0.3018	0.1352	2.23225	0.4823	0.2163	17
C2	C9	OH	0.3018	0.1352	2.23225	0.4823	0.2163	17
C3	C10	UG	0.3018	0.1352	2.23225	0.4823	0.2163	17
C3	C11	UG	0.3018	0.1352	2.23225	0.4823	0.2163	17
C4	C12	UG	0.3018	0.1352	2.23225	0.4823	0.2163	8

OH[1]: overhead line, UG[2]: underground line

Table 1.3: Transformers parameters

Node from	Node to	Connection	V_1 (kV)	V_2 (kV)
R0	R1	1-Φ Y0-Y0	7.2 LN	0.240 LN
I0	I1	3-Φ Y0-Y0	12.47 LL	0.480 LL
C0	C1	3-Φ Y0-Y0	12.47 LL	0.208 LL

(with 3-10% grid-side inductance) and/or with transformers (with 3-10% leakage inductance), the equivalent feeder inductance and therefore the equivalent electrical distance among the DG units are comparable to those of medium and long transmission lines. The 12-40% inductance with both a grid-side inductor and a transformer between two DG units is equivalent to over 160 kilometers of transmission line, which is the average transmission distance in North America [23].

1.5 Challenges Related to Microgrid Operation

The proper operation of a microgrid requires the development of a number of technologies, for which the control strategy and protection scheme are the two most critical issues.

The control issues for a microgrid include mainly the implementation of high-performance power flow control and voltage regulation, grid synchronization, and islanding detection. Different microgrid operation modes require different control strategies. For example, in the grid-connected mode, each DG unit in a microgrid needs to generate the appropriate amount of real and reactive power (the dispatched power or the maximum available from the energy sources) [24] . In the islanding mode, the DG units supply the loads independently, and the appropriate sharing of the real and reactive power demand among the DG units is critical to ensure that no DG unit is operated beyond its maximum rating. Due to the different control strategies in different microgrid operation modes, the islanding operation detection algorithm is important for control scheme switching when the microgrid changes between the grid-connected mode and the islanding mode. Finally, the controller should also include the synchronization algorithm, which can synchronize the microgrid terminal voltage with the utility voltage before connecting the microgrid to the grid. As mentioned earlier, these control methods prefer to use the variable control locally available to each DG unit, so that communication among DG units can be avoided in order to improve the system reliability and reduce the costs [25][26][16].

On the other hand, a good protection scheme for a microgrid should ensure that the microgrid can respond quickly to faults both in the utility and inside the microgrid [23][27]. In case of a utility fault, the microgrid should be able to detect the fault and switch to the islanding operation mode instantaneously. When a fault occurs in the microgrid, the protection scheme should be able to isolate the fault by de-energizing the smallest possible amount of components of the microgrid.

1.6 Research Objective

In research for this thesis, we focused on the control of a microgrid during the islanding operation mode. Specifically, we studied the challenges of real and reactive power control and sharing among DG units in a low-voltage microgrid during the islanding operation. As was discussed in the previous section, in a low-voltage microgrid with a high R/X line impedance ratio and different DG grid connection topologies (with/without grid side inductors), the control of the power flow is difficult. Furthermore, since power control can be based on only locally available information without communication among the DG units, the development of a power control strategy for a low-voltage microgrid is challenging.

One method for the communicationless control of parallel DG units is the frequency and voltage droop method [28], which emulates the operation of parallel synchronous generators and is based on the assumption of mainly inductive line impedance. However, when implemented in a low-voltage microgrid with high R/X line impedance ratio [29], the traditional method is subject to a number of issues such as real and reactive power control coupling and deteriorated system stability.

The purpose of this thesis is to develop a new control strategy that can effectively regulate the power control and sharing among DG units in the islanding microgrid operation mode. The developed method should guarantee the system stability in a low-voltage microgrid with various combinations of equivalent line impedances and should automatically share the load demand among the DG units so that each DG will have "plug and play" characteristics.

1.7 Research Approach

In order to achieve decoupled power control in a low-voltage microgrid and to improve the system stability, a virtual frequency-voltage ($\omega - E$) frame power control strategy is proposed in this work, where the voltage and frequency are transformed into a virtual frame to obtain a completely decoupled relationship between the real and reactive power.

- The traditional voltage and frequency droop control is investigated through small signal analysis, and this method's sensitivity and stability under a low-voltage distribution system with various R/X ratios is analyzed.

- A detailed analysis of the proposed virtual frequency-voltage frame control method is presented. A comparison of the proposed method and a recently proposed virtual power frame control scheme is conducted, which reveals the superior performance of the proposed control in terms of power control accuracy, DG capacity utilization, and power quality.

- A control algorithm to guarantee that the microgrid can operate within the predetermined voltage and frequency variation limits is also proposed. Moreover, an adaptive reactive power droop method is proposed, which automatically updates the maximum reactive power limit of a DG unit based on its current rating and actual real power output and features an enlarged power output range and improved system stability.

- Simulation results and experimental results on an experimental 5 kVA microgrid prototype are obtained to verify the proposed power control strategy.

Chapter 2

Traditional Voltage and Frequency Droop Control

This chapter begins by discussing the multi-loop voltage control scheme for an inverter-based DG unit and the traditional voltage and frequency droop control method for power-sharing control among DG units in a microgrid in the islanding operation. Small signal analysis is then carried out to further investigate the performance of the traditional droop control method in a low-voltage microgrid. A recently proposed virtual real and reactive power control scheme for power decoupling is also discussed in this chapter.

2.1 Multi-loop Control Scheme for The Inverter-Based DG

This section describes the overall control scheme for inverter-based DG systems. The controller used for each DG system in the microgrid contains inner voltage and current loops for regulating the three-phase grid-interfacing inverter voltage, and external power control loops for controlling the real and reactive power outputs of the DG system (with the droop control method). The overall control scheme for the inverter-based DG is shown in Figure 2.1. If sufficient energy and storage are available at the DC link, the real and reactive power outputs of a DG system are controlled mainly through the controlling of the interfacing inverter.

2.1.1 Inner voltage and current control loops

Figure 2.1(b) shows the voltage control strategy used for controlling the three-phase grid-interfacing VSI, which contains a filter capacitor voltage control loop and a filter inductor current control loop [30][31].

The reference voltage for the inverter V_{abc}^{*} is generated from the external power loops. This voltage is then compared to the feedback voltage V_{abc} to produce the voltage error, which is then converted into the two-phase stationary $\alpha\beta$ frame and regulated with a P+ resonant controller [31][32][33][34] to reduce steady state voltage control error. The practical form of a P+ resonant controller is expressed as in (2.1):

$$G(s) = k_p + \frac{2k_i\omega_{cut}s}{s^2 + 2\omega_{cut} + \omega_0^2} \tag{2.1}$$

where k_p and k_i are the proportional and integral gains, respectively, and ω_{cut} is the controller cut-off frequency. The P+ resonant controller transforms a synchronous-

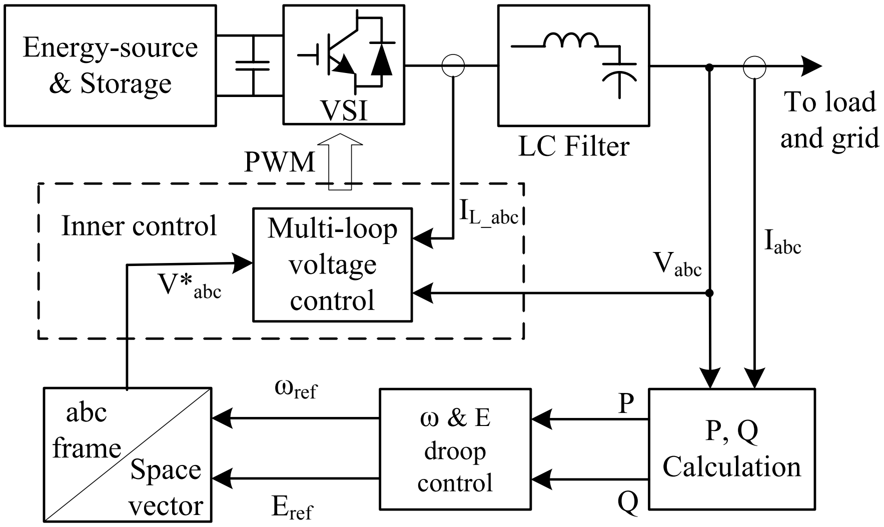

(a) Overall control scheme

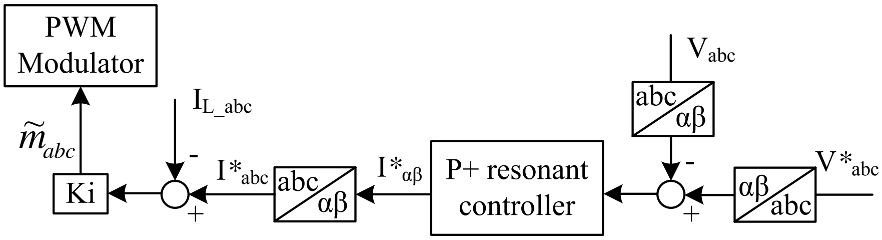

(b) Inner control

Figure 2.1: Control scheme of DG-grid interfacing inverter

frame PI controller into the stationary frame, has significant gains around the line frequency ω_0, and guarantees near zero steady-state error regulation at this frequency [31][32][33][34].

The output of the voltage control loop is the reference current (I^*_{abc}) for the current control loop. Its purpose is to improve the inverter control transient performance and stability. The current control uses a proportional controller K_i. The output of the current control loop is the three phase modulating signals ($\tilde{m}_{abc}$), which are fed

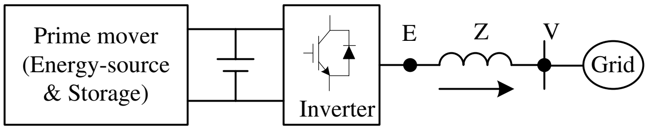

(a) Inverter interfaced DG system

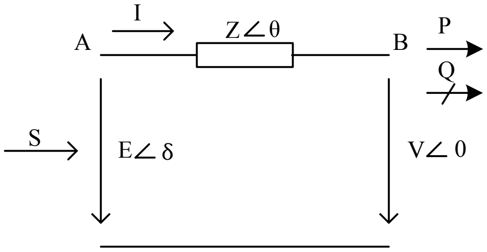

(b) Real and reactive power flows

Figure 2.2: Power flow through a line

to the pulse-width modulator (PWM) to generate the high-frequency gating signals for driving the three-phase VSI [35].

2.1.2 External real and reactive power control

The external real and reactive power control loop controls the real and reactive power output of a DG system. Traditionally, voltage and frequency droop control is implemented in the power control loops. However, before the droop control is discussed, the relationship between the DG output power and its output voltage needs to be explained first. A simplified inverter-based DG system connected to a voltage source is shown in Figure 2.2(a). Through the inner voltage and current control loop, the VSI provides control of the magnitude and phase of its output voltage E. As a result, the DG output power will be related to the DG output voltage E, the system voltage V, and the line impedance Z.

Figure 2.2(b) shows the real and reactive power flows between two voltages ($E\angle\delta$ and $V\angle 0$) separated by a line impedance ($Ze^{j\theta} = R + jX$). According to the power flows between two sources, the DG output power (sending end power) can be obtained as

$$\begin{aligned} P + jQ &= \overline{s} = \bar{E}\bar{I}^{*} \\ &= \bar{E}(\tfrac{\bar{E}-\bar{V}}{\bar{Z}})^{*} \\ &= E(\tfrac{E-Ve^{j\delta}}{Ze^{-j\theta}}) \\ &= \tfrac{E^2}{Z}e^{j\theta} - \tfrac{EV}{Z}e^{j(\theta+\delta)} \end{aligned} \tag{2.2}$$

Thus, the real and reactive power output of the DG is

$$P = \frac{E^2}{Z}cos\theta - \frac{EV}{Z}cos(\theta+\delta) \tag{2.3}$$

$$Q = \frac{E^2}{Z}sin\theta - \frac{EV}{Z}sin(\theta+\delta) \tag{2.4}$$

where $Ze^{j\theta} = R + jX$, (2.3) and (2.4) can be written as

$$P = \frac{E}{R^2+X^2}[R(E - Vcos\delta) + XVsin\delta] \tag{2.5}$$

$$Q = \frac{E}{R^2+X^2}[-RVsin\delta + X(E - Vcos\delta)] \tag{2.6}$$

(2.5) and (2.6) can be rearranged as

$$Vsin\delta = \frac{XP - RQ}{E} \tag{2.7}$$

$$E - Vcos\delta = \frac{RP + XQ}{E} \tag{2.8}$$

For traditional power flow analysis, an inductive line impedance is usually assumed with $X \gg R$ (this assumption is true when considering inductive transmission lines and numerous transformers and generators). Thus R in the above equation can be neglected. If we assume that the power angle δ is very small, we have $sin\delta = \delta$ and $cos\delta = 1$. Equations (2.7) and (2.8) can then be simplified as

$$\delta \approx \frac{XP}{EV} \tag{2.9}$$

$$E - V \approx \frac{XQ}{E} \tag{2.10}$$

Equations (2.9) and (2.10) reveal that the DG output real power is related to the phase angle difference, while the DG output reactive power depends on the voltage magnitude difference.

As controlling the frequency dynamically controls the phase angle, the real and reactive power can be controlled by adjusting the DG output frequency and voltage magnitude, respectively. Therefore, the power control loops actually generate the reference frequency and voltage magnitude for the inner voltage and current loop as illustrated in Figure 2.1(b). Figure 2.1(a) shows that the droop control is used in the power loops. The details of this droop control are presented in the following section.

2.2 Traditional Voltage and Frequency Droop Control

In an islanding microgrid with DG systems operating in parallel, the DG units must be controlled to share the total load demand according to their respective ratings to avoid DG overloads and to ensure the microgrids stable operation. The conventional frequency and voltage droop method achieves the above functions by emulating a traditional power system with parallel synchronous generators [28][36][16]. This method uses the microgrid frequency and voltage as the communication link and therefore

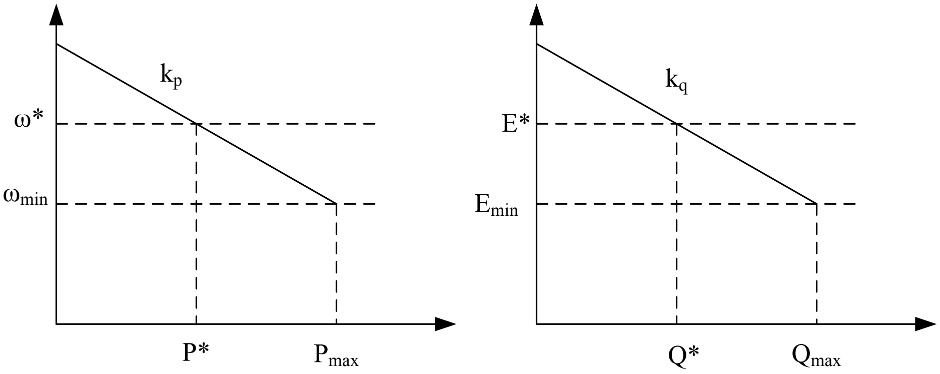

Figure 2.3: Frequency and voltage droop characteristics

enables the DG units to share the load demand without physical communications among them [37][38].

The traditional “real power versus frequency ($P-\omega$)” and “reactive power versus voltage ($Q-E$)” droop characteristics can be expressed as

$$\omega_{min} - \omega^* = -k_p(P_{max} - P^*) \tag{2.11}$$

$$E_{min} - E^* = -k_q(Q_{max} - Q^*) \tag{2.12}$$

where P_{max} and Q_{max} are the maximum real and reactive power outputs of a DG, ω_{min} and E_{min} are the minimum allowable microgrid frequency and voltage magnitude. P^* and Q^* are the dispatched powers for a DG in the grid-connected operation mode, while ω^* and E^* are the utility frequency and PCC voltage magnitude. k_p and k_q are the slopes of the $P-\omega$ and $Q-E$ droop characteristics, which are determined as in Figure 2.3. These slopes ensure a smooth microgrid transition from grid-connected mode (with outputs of P^* and Q^*) to the islanding mode operation [16].

With this droop control, all the DG systems will produce the dispatched real and reactive power in the grid-connected mode and will generate the maximum power in islanding mode under the maximum load demand. In other words, they will share the total microgrid load demand in a predetermined manner according to their respective ratings. This result is achieved without communication among the DG systems, and, therefore, the “plug and play” of a DG unit is possible under droop control.

However, this droop control is based on the relationships in (2.9) and (2.10) , where a inductive line impedance is assumed. For a low-voltage microgrid, where the equivalent impedance between any two DG systems can be either resistive or inductive (with a DG coupling transformer or a grid side inductor), the impedance resistance R can no longer be neglected. In this case, as illustrated in (2.7) and (2.8), adjusting the frequency not only influences the real power but also affects the reactive power. Similarly, adjusting the voltage affects both the real and reactive power. As a result, in a low-voltage microgrid, the traditional droop control is subject to serious power couplings and may even affect the system stability[39]. The effect of the R/X ratio on the system is analyzed in the following section by using small signal analysis.

2.3 Small Signal Model

Small signal stability is the ability of the power system to maintain synchronism under small disturbances. Such disturbances occur continually in the system because of small variations in the loads and generation. The disturbances are considered sufficiently small for the linearization of system equations to be permissible for purposes of analysis [40][41].

The small signal analysis of parallel connected inverter-based DG system using the traditional droop power control method is conducted in this section. The overall control scheme for each DG system is shown in Figure 2.1, where the interfacing inverter is controlled with an inner multi-loop control with a filter inductor current loop and a filter capacitor voltage loop. The sinusoidal reference for the inverter voltage control is obtained from the reference frequency and voltage magnitude produced by the power control scheme. The real and reactive power control is realized by the $P-\omega$, $Q-E$ droop control.

For the control scheme in Figure 2.1, it is reasonable to assume that the inverter voltage and current control loops are much faster than the outer real and reactive power control loops, and therefore can be assumed to be a unity gain. Following a similar small signal analysis procedure as that in [42][43], the power control dynamic and stability can be analyzed by examining the homogeneous equations and the root loci plots [44][45].

By using the $P-\omega$ and $Q-E$ droop control with the islanding operation mode, the DG unit output frequency ω and output voltage E will be controlled by the droop characteristics defined by equations (2.13) and (2.14), respectively:

$$\omega = \omega^* - k_p(P - P^*) \tag{2.13}$$

$$E = E^* - k_q(Q - Q^*) \tag{2.14}$$

The real power and the reactive power at the output of the interfacing inverter are given by equations (2.15) and (2.16):

$$P = \frac{1}{R^2+X^2}(RE^2 - REV\cos\delta + XEV\sin\delta) \tag{2.15}$$

$$Q = \frac{1}{R^2+X^2}(XE^2 - XEV\cos\delta - REV\sin\delta) \tag{2.16}$$

For the small disturbances around the equilibrium point defined by (δ_e, E_e, V_e), the linearized equations in (2.17 - 2.20) can be obtained:

$$\begin{aligned}
\triangle\omega &= \frac{\partial\omega}{\partial P}\triangle P && (2.17)\\
\triangle E &= \frac{\partial E}{\partial Q}\triangle Q && (2.18)\\
\triangle P &= \frac{\partial P}{\partial E}\triangle E + \frac{\partial P}{\partial \delta}\triangle\delta && (2.19)\\
\triangle Q &= \frac{\partial Q}{\partial E}\triangle E + \frac{\partial Q}{\partial \delta}\triangle\delta && (2.20)
\end{aligned}$$

where $\triangle$ denotes the small deviation of the variable from the equilibrium point. Substituting P and Q into (2.13) and (2.14) and calculating the partial derivatives by using (2.15) and (2.16), we get

$$\begin{aligned}
\triangle\omega &= -k_p\triangle P && (2.21)\\
\triangle E &= -k_q\triangle Q && (2.22)\\
\triangle P &= k_{pe}\triangle E + k_{pd}\triangle\delta && (2.23)\\
\triangle Q &= k_{qe}\triangle E + k_{qd}\triangle\delta && (2.24)
\end{aligned}$$

where

$$\begin{aligned}
k_{pe} &= \frac{\partial P}{\partial E} = \frac{1}{R^2+X^2}(2RE - RV\cos\delta + XV\sin\delta) && (2.25)\\
k_{pd} &= \frac{\partial P}{\partial \delta} = \frac{1}{R^2+X^2}(REV\sin\delta + XEV\cos\delta) && (2.26)\\
k_{qe} &= \frac{\partial Q}{\partial E} = \frac{1}{R^2+X^2}(2XE - XV\cos\delta - RV\sin\delta) && (2.27)\\
k_{qd} &= \frac{\partial Q}{\partial \delta} = \frac{1}{R^2+X^2}(XEV\sin\delta - REV\cos\delta) && (2.28)
\end{aligned}$$

To measure the output of the real and reactive power of the inverter for the power feedback control in (2.13) and (2.14), a low pass filter is usually used. Thus, the real and reactive output power obtained by measurement can be represented by equations

Table 2.1: System parameters for the small signal analysis

Variable	Value	Unit
Line impedance ($z\angle\theta$)	$1\angle 85^\circ$	Ω
Cut-off frequency of measuring filter (ω_f)	37.7	rad/s
Frequency C real power droop slope (k_p)	0.01	rad/s/W
Voltage C reactive power droop slope (k_q)	0.033	V/Var

(2.29) and (2.30), where ω_f is the cut-off frequency of the low pass filter:

$$\triangle P_{mes}(s) = \frac{\omega_f}{s + \omega_f} \triangle P(s) \tag{2.29}$$

$$\triangle Q_{mes}(s) = \frac{\omega_f}{s + \omega_f} \triangle Q(s) \tag{2.30}$$

As the inner voltage and current control bandwidth are much higher than the output real and reactive power control loops (mainly due to the low cut-off frequency of the power measurement in a low pass filter), it is reasonable to consider the inverter as an ideal voltage source with controllable amplitude and frequency. Therefore, we get the following equations

$$\triangle\omega(s) = -\frac{k_p\omega_f}{s + \omega_f}(k_{pe}\triangle E(s) + k_{pd}\triangle\delta(s)) \tag{2.31}$$

$$\triangle E(s) = -\frac{k_q\omega_f}{s + \omega_f}(k_{qe}\triangle E(s) + k_{qd}\triangle\delta(s)) \tag{2.32}$$

By rearranging (2.31) and (2.32), the following equation can be obtained:

$$\triangle\omega(s) = -\frac{k_p\omega_f}{s + \omega_f}(k_{pd}\triangle\delta(s) - \frac{k_q k_{pe} k_{qd}\omega_f}{s + \omega_f + k_q k_{qe}\omega_f}\triangle\delta(s)) \tag{2.33}$$

Since the phase angle is indeed the integration of the frequency:

$$\triangle\omega(s) = s\triangle\delta(s) \tag{2.34}$$

if we replace the frequency in (2.33) by (2.34), we have a homogeneous equation as in (2.35):

$$s^3\triangle\delta(s) + as^2\triangle\delta(s) + bs\triangle\delta(s) + c\triangle\delta(s) = 0 \tag{2.35}$$

where

$$a = (2 + k_q k_{qe})\omega_f \tag{2.36}$$

$$b = (k_p k_{pd} + k_q k_{qe}\omega_f + \omega_f)\omega_f \tag{2.37}$$

$$c = (k_{pd} + k_q k_{pd} k_{qe} - k_q k_{pe} k_{qd}) k_p \omega_f^2 \tag{2.38}$$

The homogeneous equation (2.35) describes the free motion of the system for small disturbances around the equilibrium point (δ_e, E_e, V_e). Thus, the system response can be analyzed by using the characteristics equation (2.39):

$$\lambda^3 + a\lambda^2 + b\lambda + c = 0 \tag{2.39}$$

2.4 Stability Analysis

In order to understand the dynamic behavior of the system, some root loci plots are shown as a function of the given system parameters, which are listed in Table 2.1.

Figure 2.4 shows the root loci plot for the system with a variation of the line impedance angle θ ($Z = z\angle\theta$) from 85° to 5°, so that the line impedance changes from inductive to resistive. The system has three roots: one real pole ($\lambda 1$) and two conjugated poles ($\lambda 2$ and $\lambda 3$). The arrow lines indicate the evolution of the corresponding pole when the angle decreases. As Figure 2.4 showns, with the angle θ decrease, all the three poles go toward the imaginary axis. Finally, the two conjugated poles cross the imaginary axis and stay in the right side of the s-plane. The system

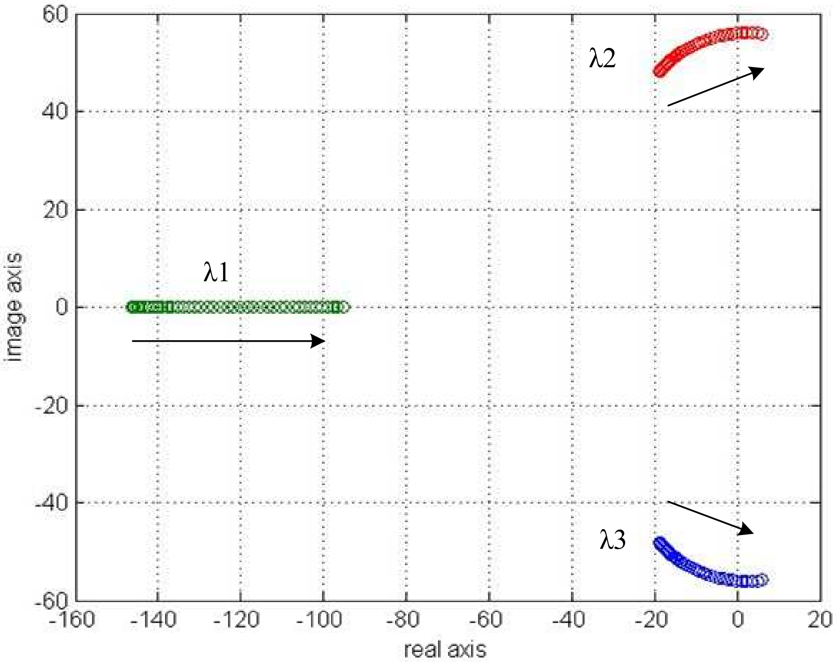

Figure 2.4: θ changes from 85° to 5°

obviously becomes unstable with a smaller θ. In other words, the system has better stability with inductive line impedance, while the system becomes less stable and finally unstable with resistive line impedance.

Figure 2.5 shows the root loci plot for the system with a variation of reactance X from 0.1 to 7 Ω, while resistance R retains constant at 0.7 Ω. When the line inductance is too small, the system is obviously unstable with two poles in the right half plane. However, when the line inductance becomes dominant, the two dominant poles ($\lambda 2$ and $\lambda 3$) move toward the left and close to the real axis, so the system has better stability and less power coupling.

Figure 2.6 shows the root loci plot for the system under the variation of the $P-\omega$ droop slope k_p, when $R/X = 1$. As shown, the system has better stability with lower values of the slope k_p. A higher slope k_p implies larger frequency changes, as well,

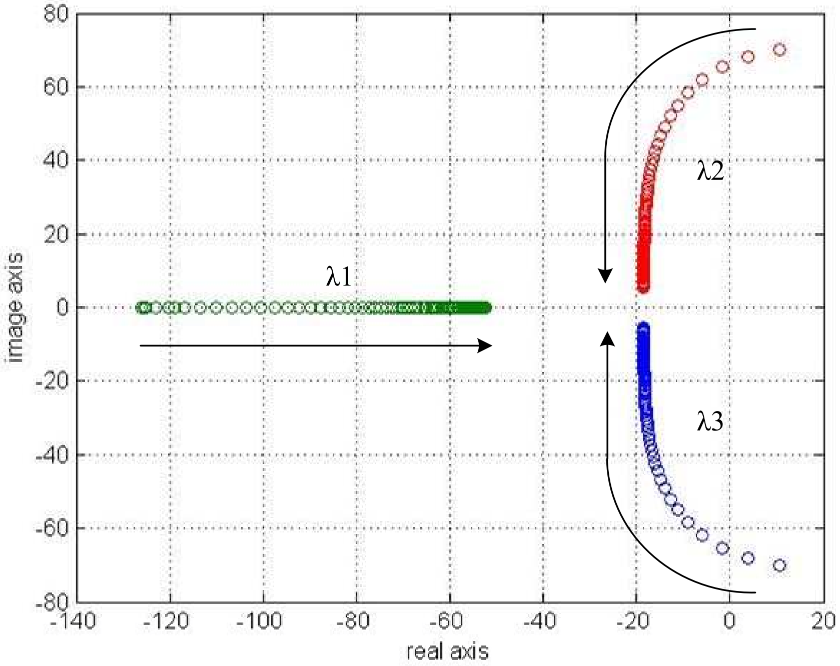

Figure 2.5: X changes from 0.1 to 7 Ω

the small-signal model does not represent the system very well [42].

Figure 2.7 shows the root loci plot for the system as a function of the variation of the $Q-E$ droop slope k_q, when $R/X = 1$. This figure reveals that the pair of complex-conjugate dominant poles $\lambda 2$ and $\lambda 3$ both move away from the real axis, so the system has an underdamped response for higher values of the parameter k_q, and the pole at $\lambda 1$ moves toward left with higher values of k_q.

Figure 2.8 shows the root locus plot for the system as a function of the measuring filter's cut-off frequency (ω_f) in the range from 37.7 to 377 rad/s. The system becomes underdamped for lower values of the cut-off frequency, and the system has a faster response with a higher cut-off frequency.

The above analysis reveals that the system damping and stability are sensitive to the droop slopes, power measurement low pass filter cut-off frequency, and the line

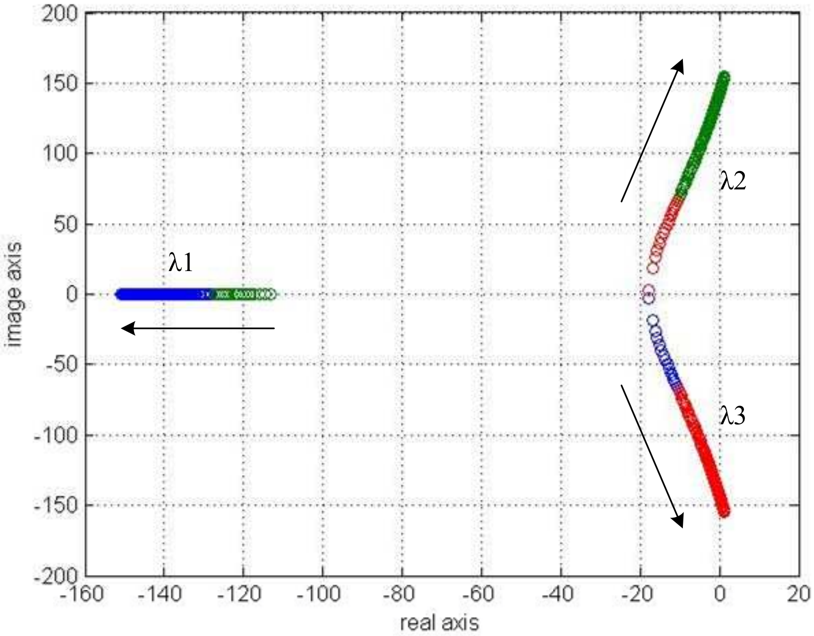

Figure 2.6: k_p changes from 0.001 to 0.1

impedance parameters. However, the line impedance has the most obvious effects as it directly influences the power flows. With an increase in the line impedance R/X ratio, the system damping becomes worse, and the system eventually becomes unstable.

2.5 Virtual $P-Q$ Frame Droop Control

As in the previous analysis showed, when the traditional droop control method is implemented in a low-voltage microgrid, where the line impedance is no longer inductive, the system will have some problems such as serious real and reactive power control coupling and deteriorated system stability. In this case, the droop control scheme described by (2.11) and (2.12) is no longer effective.

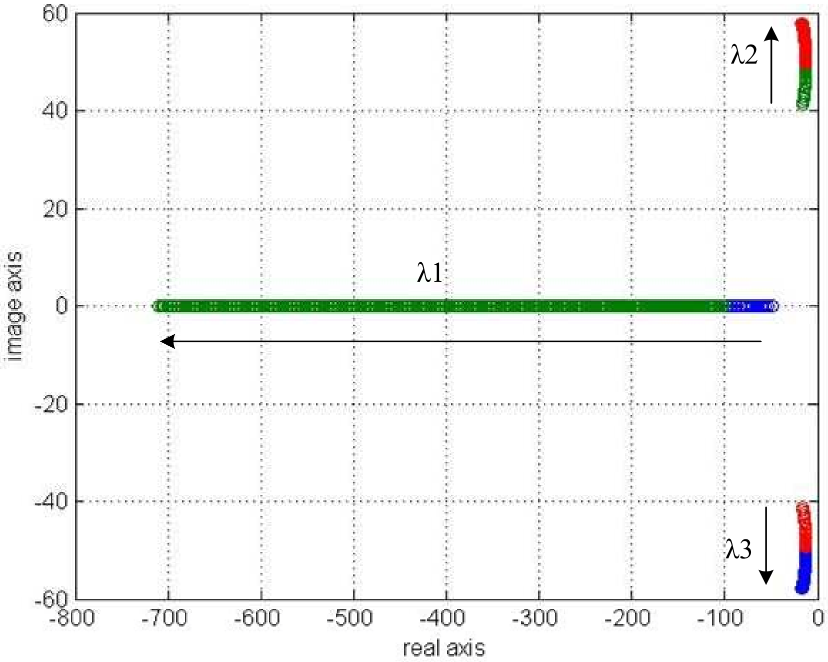

Figure 2.7: k_q changes from 0.003 to 0.3

Generally, to decouple the power flow control, both the reactance X and resistance R of the line impedance need to be considered. In [46], a method is proposed to solve this power-coupling problem by using an orthogonal frame transformation that transforms the actual real and reactive power (P and Q) into the virtual real and reactive power (P' and Q'). This $P-Q$ frame transformation can be realized by

$$\begin{bmatrix} P' \\ Q' \end{bmatrix} = T_{PQ} \begin{bmatrix} P \\ Q \end{bmatrix} \tag{2.40}$$

where

$$T_{PQ} = \begin{bmatrix} \cos\alpha & -\sin\alpha \\ \sin\alpha & \cos\alpha \end{bmatrix} = \begin{bmatrix} \frac{X}{Z} & \frac{-R}{Z} \\ \frac{R}{Z} & \frac{X}{Z} \end{bmatrix} \tag{2.41}$$

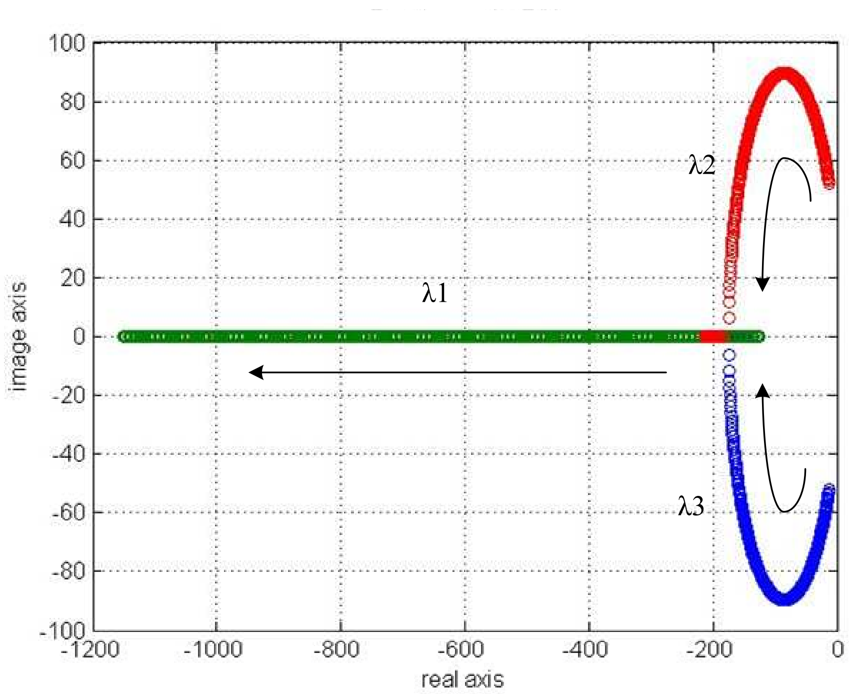

Figure 2.8: ω_f changes from 37.7 to 377 rad/s

Applying the transformation presented in (2.40) on (2.5) and (2.6) results in

$$\sin\delta = \frac{ZP'}{EV} \tag{2.42}$$

$$E - V\cos\delta = \frac{ZQ'}{E} \tag{2.43}$$

By using this method, the relationship in (2.7) and (2.8) can be updated as (2.42) and (2.43), which show that the virtual real power P' depends only on the power angle δ, while the virtual reactive power Q' depends only on the voltage amplitude E. In other words, the virtual real power P' can be controlled by regulating the power angle δ, whereas the virtual reactive power Q' can be controlled through the inverter voltage E. Therefore, the transformation matrix T_{PQ} represented in (2.41) can achieve the decoupled power control. This transformation is illustrated graphically in Figure (2.9). The effect of the voltage and frequency on P', Q', P,

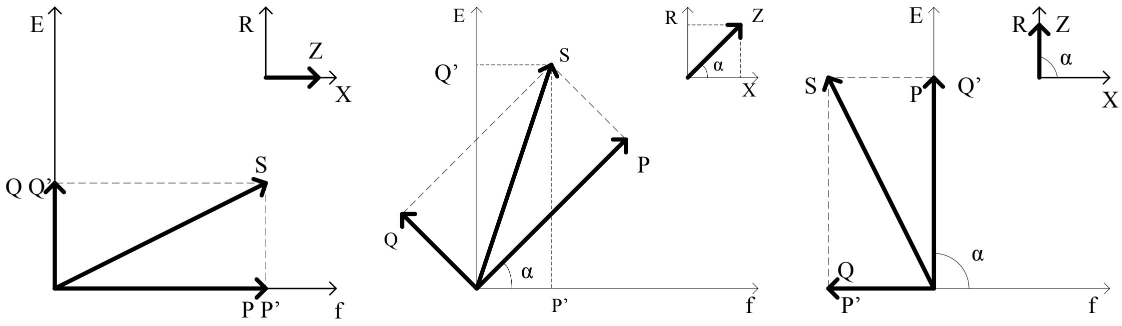

Figure 2.9: Influence of voltage and frequency on real power and reactive power for different line impedance ratios: (a)$R/X=0$, (b)$R/X=1$, (c)$R/X=\infty$

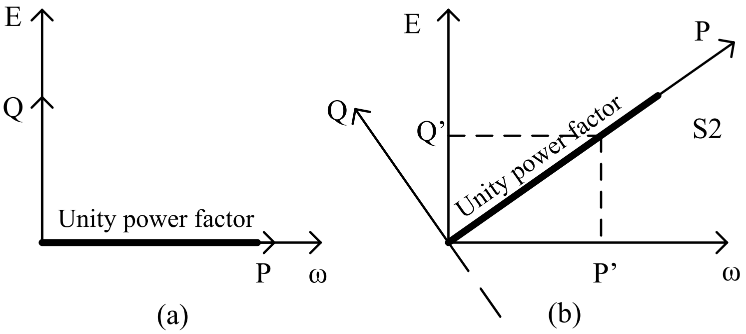

Figure 2.10: Real power control in PQ frame transformation

and Q is illustrated for different ratios of R/X.

However, with the virtual power being the directly controlled variable, the power sharing control in this method cannot guarantee that the actual real and reactive power demands in the microgrid will be properly shared between the DG units. This problem leads to a number of complications such as difficulties in predictable power sharing and DG unit output power range variations. A simple and obvious example is the unity power factor power injection. Without the virtual power transformation, only the frequency (ω) control is sufficient to regulate the real power while the voltage magnitude (E) is fixed to ensure $Q = 0$, as shown in Figure 2.10 (a). However, in the virtual power ($P'-Q'$) frame as shown in Figure 2.10 (b), both P' and Q' (therefore ω and E) must be controlled simultaneously to satisfy the requirement for a unity power factor ($Q = 0$). This requirement implies that a complex power control strategy incorporating both the virtual power control and actual power control requirements must be developed. On the other hand, in the virtual power frame, as the virtual power operation range must be determined by the actual real and reactive power range, the operation range's inconsistency in different frames will result in the over-rating or under-rating of a DG unit. A comparison of this virtual power frame control and the proposed control scheme is provided in the next chapter.

2.6 Summary

In this chapter, the traditional droop control scheme of DG units in a microgrid was reviewed. This control method is based on the assumption of mainly inductive line impedance, and when implemented in a low-voltage microgrid, is subject to real and reactive power coupling and system stability concerns. A small signal model of a inverter-interfaced DG system with droop control was also developed, and the root loci analysis confirmed the above conclusions.

In order to decouple the power flow control in a low-voltage microgrid, the virtual power frame control proposed in [46] was also reviewed in this chapter. This method modifies the droop control by considering both the line resistance and inductance. However, this method has a few drawbacks such as the indirect control of power and DG operation range variation. Inspired by the working principle of the $P - Q$ frame transformation method, we proposed a new power control method for power control decoupling. The details of the proposed method and the associated control algorithms are presented in the next chapter.

Chapter 3

Proposed Virtual $\omega - E$ Frame Power Control Scheme

To achieve decoupled real and reactive power control and improved low-voltage microgrid system stability, and inspired by the working principle of the virtual real power-reactive power frame transformation discussed in Chapter 2, we propose in this chapter a novel virtual frequency-voltage ($\omega' - E'$) frame transformation. The details of the $\omega' - E'$ frame control scheme and a small signal stability analysis are presented. Furthermore, an adaptive reactive power droop method that can optimally utilize the rating of a DG is also presented in this chapter.

3.1 Virtual $\omega - E$ Frame Transformation

With a further check of the droop characteristics defined by equations (2.13) and (2.14), we can find that, instead of the frame transformation of the real and reactive power, the power control decoupling can be achieved by transforming the voltage

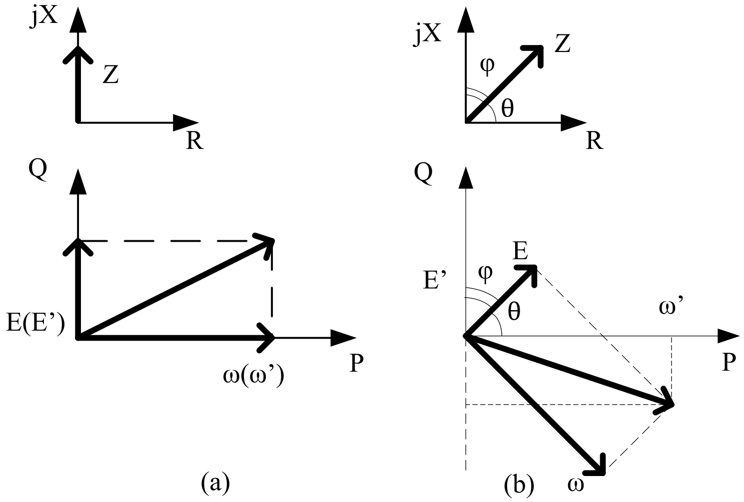

Figure 3.1: $\omega - E$ frame transformation (a)$R/X = 0$, (b)$R/X = 1$

(E) and frequency (ω) into a new frame. With the $\omega - E$ frame transformation, the actual real and reactive power can be directly controlled. As a result, the DG unit output power control and sharing can be realized without power coupling, and, at the same time, the DG output power range can be accurately controlled.

Figure 3.1 shows the principle of the proposed $\omega - E$ frame transformation. The line impedance is represented as $Ze^{j\theta} = R + jX$, where θ is the impedance angle. Figure 3.1 (a) reveals that when the line impedance is inductive ($\theta = 90^\circ$), no power coupling occurs, so that P is completely determined by ω, and Q is completely determined by E. However, when both line resistance and reactance are present as shown in Figure 3.1 (b), coupling appears between the real and reactive power flows, so that the frequency influences both the real and reactive power. Similarly, in such a case, adjusting voltage magnitude also influences both the real and reactive power. To achieve power decoupling, the $\omega - E$ frame is rotated by an angle of φ ($\varphi = 90^\circ - \theta$) to the new virtual $\omega - E$ frame, as illustrated in Figure 3.1 (b). This

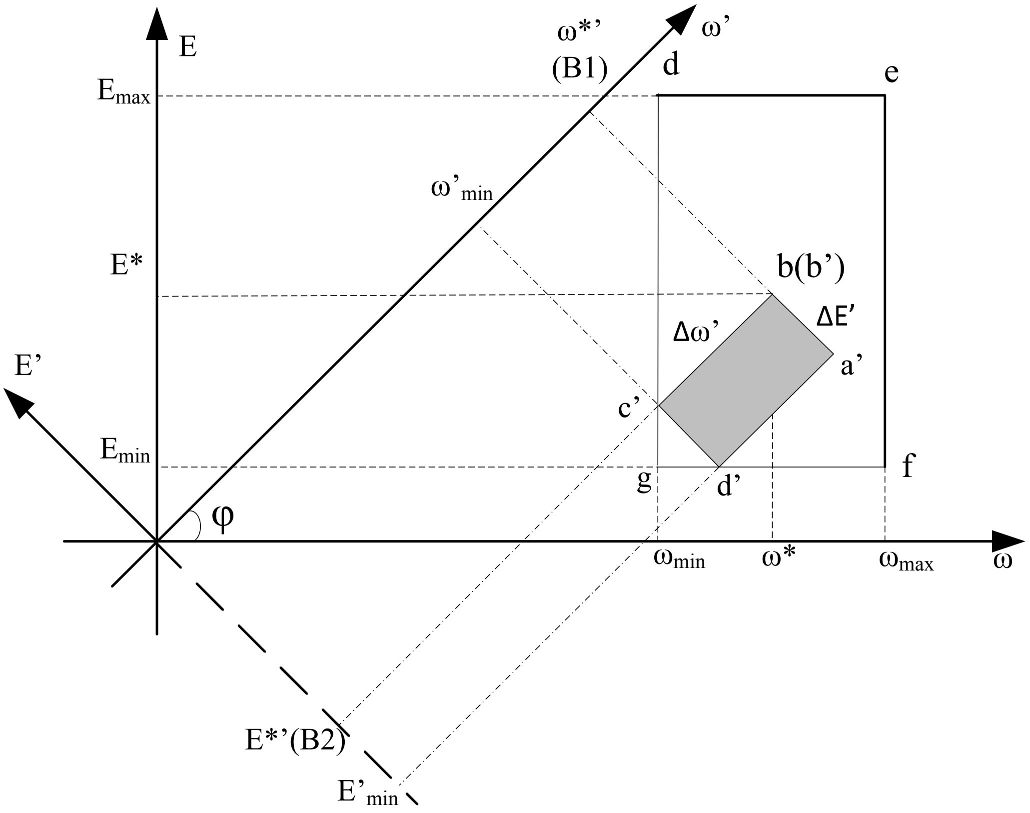

Figure 3.2: Details of the $\omega - E$ frame transformation

orthogonal frame rotation can be achieved by using a frame transformation matrix $T_{\omega E}$ as in (3.1):

$$\begin{bmatrix} \omega' \\ E' \end{bmatrix} = T_{\omega E} \begin{bmatrix} \omega \\ E \end{bmatrix} \tag{3.1}$$

where

$$T_{\omega E} = \begin{bmatrix} \cos\varphi & \sin\varphi \\ -\sin\varphi & \cos\varphi \end{bmatrix} \tag{3.2}$$

Figure 3.2 shows the details of the $\omega - E$ frame transformation. In the new $\omega' - E'$ frame, the real power and the reactive power are shared based on the virtual frequency (ω') and virtual voltage (E'), respectively. To ensure that each DG unit

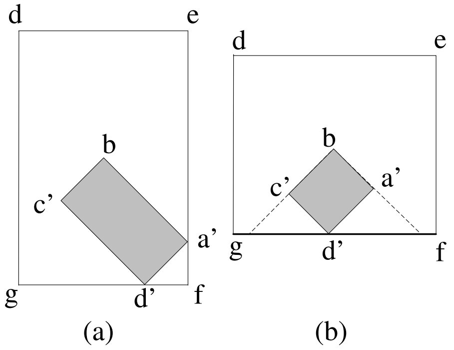

Figure 3.3: Possible operation range in the $\omega' - E'$ frame

operates within the allowable voltage and frequency limits, the DG operation range in the $\omega' - E'$ frame should be within the voltage and frequency limits set in the original $\omega - E$ frame, which is the rectangle determined by d (ω_{min}, E_{max}), e (ω_{max}, E_{max}), f (ω_{max}, E_{min}) and g (ω_{min}, E_{min}). As a result, the shaded area in Figure 3.2 is the new operation range corresponding to an increase in both P and Q demands when the microgrid is transferred from the grid-connected operation mode (point b in $\omega - E$ frame or b' in $\omega' - E'$ frame) to the islanding operation mode. Compared to the $P - Q$ operation range's inconsistency in the virtual power frame control, the new frequency and voltage operation range will not affect the power output limits of a DG unit.

Although Figure 3.2 shows that the left and bottom boundaries (ω_{min} and E_{min}) in the original operation range are used to determine the new operation range in the virtual frame corresponding to an increase in both the real and reactive power, numerous other methods can be used to determine the new rectangular operation range in the $\omega' - E'$ frame. However, as the largest possible range is usually desired, the boundary of the original operation range in the $\omega - E$ frame preferably should

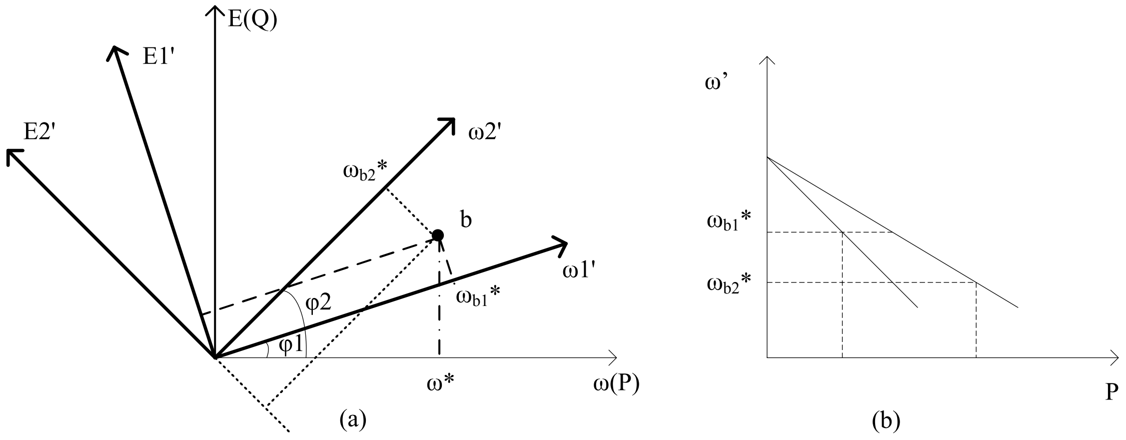

(a) (b)

Figure 3.4: Two DG units have different frame transformation angles, (a) frame transformation, (b) droop control on the virtual frame.

be used for the new range determination. Two other possible examples are shown in Figure 3.3, where the new operation range (the shaded area) in Figure 3.3 (a) is determined by the right boundary (ω_{max}) and the bottom boundary (E_{min}) of the original rectangular range. Figure 3.3 (b) illustrates the situation in which the virtual frequency and voltage could not reach the left or right boundaries of the original rectangle. Since only the bottom boundary (E_{min}) is available, an additional criterion (such as similar rectangles) needs to be used to determine the new operation range. In the $\omega' - E'$ range determination, the priority of greater virtual frequency range or virtual voltage range could also be properly considered. A further discussion of the operation range determination is presented in Section 3.4.

In a microgrid with many DG units operating in parallel, one possible complication from using the virtual frame power control is that if the frame transformation angle (φ) is not the same for all the DG units in a microgrid, the microgrid frequency and voltage will be converted to different values in different virtual frames. Figure

3.4 shows two DG units operating with different frame transformation angles, where DG1 has a transformation angle of $\varphi 1$, and DG 2 has a transformation angle of $\varphi 2$. Obviously, the same operating point b in the actual frame will be different in the virtual frames, and, as a result, the virtual frequency and voltage for DG1 and DG2 will not be consistent, as shown in Figure 3.4 (b). For this reason, the virtual frequency or voltage cannot be used as an effective communication link for power sharing. Therefore, to ensure that the virtual frame control functions properly, the frame transformation angle (φ) for each DG unit should be the same, and, in this thesis, the rotation angle φ is chosen as 45° (corresponding to the ratio $R/X = 1/1$), which can ensure a reasonably good performance for a microgrid with both directly coupled DG systems (no additional output inductance) and DG systems with output transformers or LCL filters (with grid side inductors).

3.2 Comparison with The Virtual $P-Q$ Frame Control

A comparison of the proposed virtual $\omega - E$ frame control with the virtual $P-Q$ control in [46] reveals that these two types of frame transformation are similar in terms of frame transformation for power flow decoupling. However, a further comparison reveals that the proposed $\omega - E$ frame control has a few important advantages:

- *Direct real and reactive power control.* By controlling the virtual voltage and frequency, the proposed method can share the real and reactive power directly. For the virtual real and reactive power control scheme, controlling the actual real and reactive power is not straightforward, a complex control algorithm is needed even for unity power factor control, as discussed in Chapter 2.

- *Reduction of operation range.* In the proposed virtual $\omega - E$ frame control, the voltage and frequency operation range is shrunk to make sure that the virtual frequency and voltage control will not lead to an operation point out of the microgrid's preset frequency and voltage range. This reduction of the frequency and voltage range actually benefits the power quality. Similarly, the virtual $P - Q$ frame control will also need a reduction of the power output range for a similar reason. However, this reduction of output power will result in the inefficient operation of a DG system.

- *Power-sharing accuracy.* With the straightforward control of the real and reactive power, and with the newly defined virtual frequency and voltage range, the new droop slopes for power control are determined according to the virtual $\omega - E$ frame control. Therefore, the power sharing is accurate and is directly related to each DG unit's rating. In contrast, in the virtual $P - Q$ frame control, only the virtual power is shared, so that the reactive power output will affect the accuracy of the real power sharing, and the real power output will also affect the accuracy of reactive power sharing.

The third point can be proved by developing the droop equations corresponding to the virtual power control, as shown in (3.3) and (3.4) (α is the virtual power frame transformation angle; see Figure 2.9):

$$\omega = \omega^* - k_p \cdot \cos\alpha \cdot (P - P^*) + k_p \cdot \sin\alpha \cdot (Q - Q^*) \tag{3.3}$$

$$E = E^* - k_q \cdot \cos\alpha \cdot (Q - Q^*) + k_q \cdot \sin\alpha \cdot (P - P^*) \tag{3.4}$$

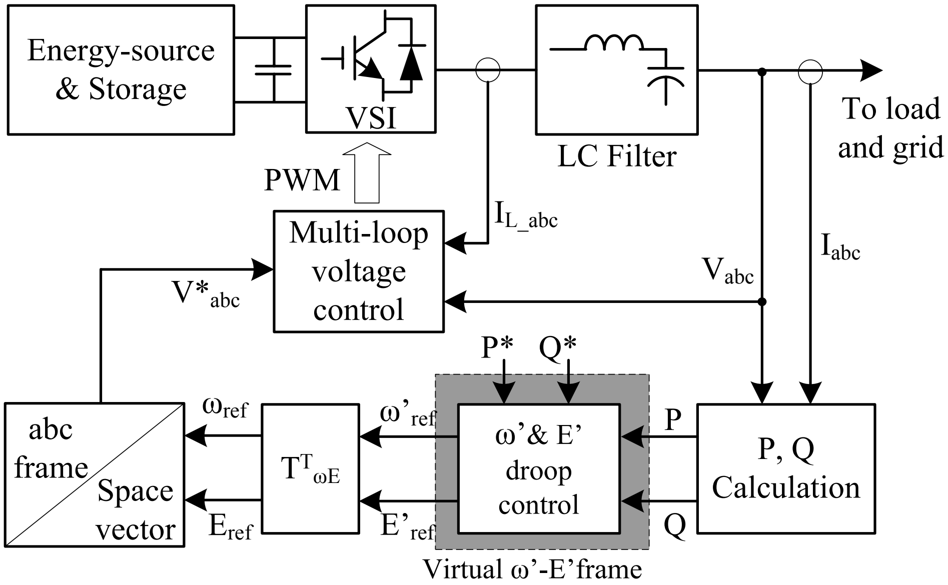

Figure 3.5: The overall control scheme with $\omega - E$ frame transformation

where the third term in both equations obviously will affect the real and reactive power-sharing performance. This power-sharing inaccuracy resulting from using the virtual $P - Q$ frame was also identified recently in [47].

3.3 Virtual $\omega - E$ Frame Control Stability Analysis

The small signal analysis of a parallel connected inverters system using the traditional droop power control method was reviewed in Chapter 2. The overall control scheme for each DG system, shown in Figure 3.5, is similar to that shown in Figure 2.1, with the only difference being that the virtual frequency-voltage frame transformation is implemented in the power control loops. As shown in Figure 3.5, similar to the traditional droop control, the sinusoidal reference for the inverter voltage control is obtained from the reference frequency and voltage magnitude produced by the power control scheme. The real and reactive power control is realized in the block with the virtual $\omega - E$ frame. The virtual frame variables are transformed back to the actual frequency and voltage reference for the inverter control by using the inverse transformation matrix $T_{\omega E}^T$:

$$T_{\omega E}^T = \begin{bmatrix} \cos\varphi & -\sin\varphi \\ \sin\varphi & \cos\varphi \end{bmatrix} \tag{3.5}$$

Similarly, for the control scheme in Figure 3.5, it is reasonable to assume that the inverter voltage and current control loops are much faster than the outer real and reactive power control loops, and therefore can be assumed to be a unity gain. By following a similar small signal analysis procedure to that presented in Chapter 2, the power control dynamic and stability can be analyzed by examining the homogeneous equations and the root locus plots.

For the convenience of analysis, we use the shaded area shown in Figure 3.2 as the new operation range in the $\omega' - E'$ frame as an example. As discussed earlier, the droop slopes k_p and k_q presented in equations (2.11) and (2.12) are determined as

$$k_p = \frac{\omega^* - \omega_{min}}{P^* - P_{max}} = \frac{\Delta\omega}{\Delta P} \tag{3.6}$$

$$k_q = \frac{E^* - E_{min}}{Q^* - Q_{max}} = \frac{\Delta E}{\Delta Q} \tag{3.7}$$

The virtual frequency and voltage droop slopes (k_p' and k_q') in the $\omega' - E'$ frame can therefore be determined by finding $\Delta\omega'$ and $\Delta E'$ in the virtual frame, as in (3.8) and (3.9):

$$\Delta\omega' = \frac{\omega^* - \omega_{min}}{\cos\phi} \tag{3.8}$$

$$\Delta E' = \left| \frac{(E^* - E_{min})\cos\varphi - (\omega^* - \omega_{min})\sin\varphi}{\cos^2\varphi} \right| \tag{3.9}$$

For the other types of $\omega' - E'$ operation range, $\Delta\omega'$ and $\Delta E'$ will be different from (3.8) and (3.9). However, a analysis method similar to that presented here can be used to obtain the new slopes of k'_p and k'_q.

For the virtual frequency and voltage droop slopes, the droop characteristics equations with the frequency-voltage frame transformation are represented as

$$\begin{aligned} \omega' &= \omega^{*\prime} - k'_p(P - P^*) \qquad (3.10) \\ E' &= E^{*\prime} - k'_q(Q - Q^*) \qquad (3.11) \end{aligned}$$

For small disturbances around the equilibrium point by (δ_e, E_e, V_e), the linearized equations for the frequency and voltage magnitude can be obtained:

$$\begin{aligned} \Delta\omega'(s) &= -\frac{k'_p\omega_f}{s+\omega_f}(k_{pe}\Delta E'(s) + k_{pd}\Delta\delta'(s)) = \Delta\omega\cos\varphi + \Delta E\sin\varphi \qquad (3.12) \\ \Delta E'(s) &= -\frac{k'_q\omega_f}{s+\omega_f}(k_{qe}\Delta E'(s) + k_{qd}\Delta\delta'(s)) = \Delta E\cos\varphi - \Delta\omega\sin\varphi \qquad (3.13) \end{aligned}$$

where ω_f is the cut-off frequency of the low pass filter for use with the power measurement and

$$\begin{aligned} k_{pe} &= \frac{\partial P}{\partial E} = \frac{1}{R^2+X^2}(2RE - RV\cos\delta + XV\sin\delta) \\ k_{pd} &= \frac{\partial P}{\partial \delta} = \frac{1}{R^2+X^2}(REV\sin\delta + XEV\cos\delta) \\ k_{qe} &= \frac{\partial Q}{\partial E} = \frac{1}{R^2+X^2}(2XE - XV\cos\delta - RV\sin\delta) \\ k_{qd} &= \frac{\partial Q}{\partial \delta} = \frac{1}{R^2+X^2}(XEV\sin\delta - REV\cos\delta) \end{aligned}$$

Rearranging (3.12) and (3.13) and with $\Delta\omega'(s) = s\Delta\delta'(s)$, we have the following homogeneous equation:

$$s^3\triangle\delta(s) + as^2\triangle\delta(s) + bs\triangle\delta(s) + c\triangle\delta(s) = 0 \qquad (3.14)$$

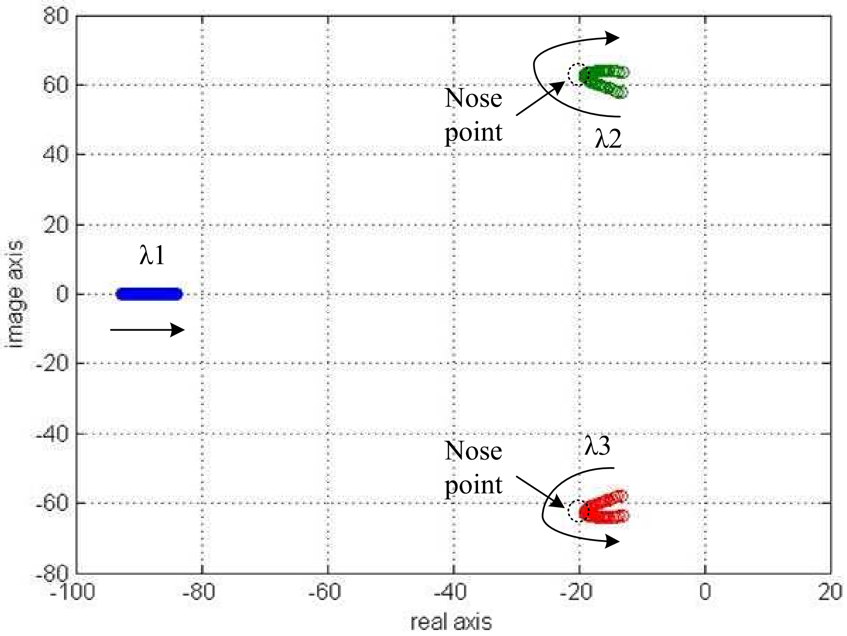

Figure 3.6: Root loci of θ changes from 85° to 5° with virtual $\omega - E$ frame control.

where

$$\begin{aligned} a &= (2 + k_p' k_{pe} \sin\varphi + k_q' k_{qe} \cos\varphi)\omega_f \\ b &= (k_p' k_{pd} \cos\varphi - k_q' k_{qd} \sin\varphi + \omega_f k_p' k_{pe} \sin\varphi + \omega_f k_q' k_{qe} \cos\varphi + \omega_f)\omega_f \\ c &= (k_p' k_{pd} \cos\varphi - k_q' k_{qd} \sin\varphi + k_p' k_q' k_{pd} k_{qe} - k_p' k_q' k_{pe} k_{qd})\omega_f^2 \end{aligned}$$

Thus, the system response can be analyzed by using the characteristics equation (3.15)

$$\lambda^3 + a\lambda^2 + b\lambda + c = 0 \tag{3.15}$$

Root locus plots are obtained to show that the virtual frequency-voltage control can improve the system dynamics and stability.

Figure 3.6 shows the root locus plots for the virtual frame control with different impedance angles θ. As this figure reveals, when the impedance angle changes from

85° to 5° (or when the impedance changes from mainly inductive to mainly resistive), all the three poles stay in the left half-plane, and the system stability is maintained. By comparing Figure 3.6 with Figure 2.4 in Chapter 2, where two of the three poles will eventually move to the right half-plane with traditional droop control, it can be verified that the system stability can be greatly improved with the proposed virtual frame control. Figure 3.6 also reveals that the two dominant poles ($\lambda 2$ and $\lambda 3$) reach the nose points at around $\theta = 45°$ ($R/X = 1$). This result is consistent with the selected frame transformation angle of $\varphi = 45°$. As shown, with a transformation angle of $\varphi = 45°$, the system stability is maintained for either mainly resistive or mainly inductive line impedance, and therefore the virtual $\omega - E$ frame control is also proved to be suitable for DG systems with significant inductive output impedance (e.g., with a coupling transformer or a LCL filter with a grid side inductor).

Figure 3.7 shows the root locus plots for the virtual $\omega - E$ frame power control with the variation of the reactance X value from 0.1 Ω to 7 Ω and a constant resistance R value of 0.7 Ω. As shown, the system stability is maintained as all the three poles stay in the left half-plane. Once again, compared to the performance of traditional droop control shown in Figure 2.5 in Chapter 2, where the system becomes unstable ($\lambda 2$ and $\lambda 3$ are in the right half-plane) when X value is too small, the performance of the proposed virtual frame droop control exhibits superior dynamics and stability.

The above analysis shows that the system stability is improved by using the virtual $\omega - E$ frame power control. However, this virtual frame control scheme also requires a careful determination of the operation range in the new $\omega' - E'$ frame. The basic requirement is that the operation range of the $\omega' - E'$ frame should be inside the preset operation range in the original $\omega - E$ frame. Otherwise, the DG will be

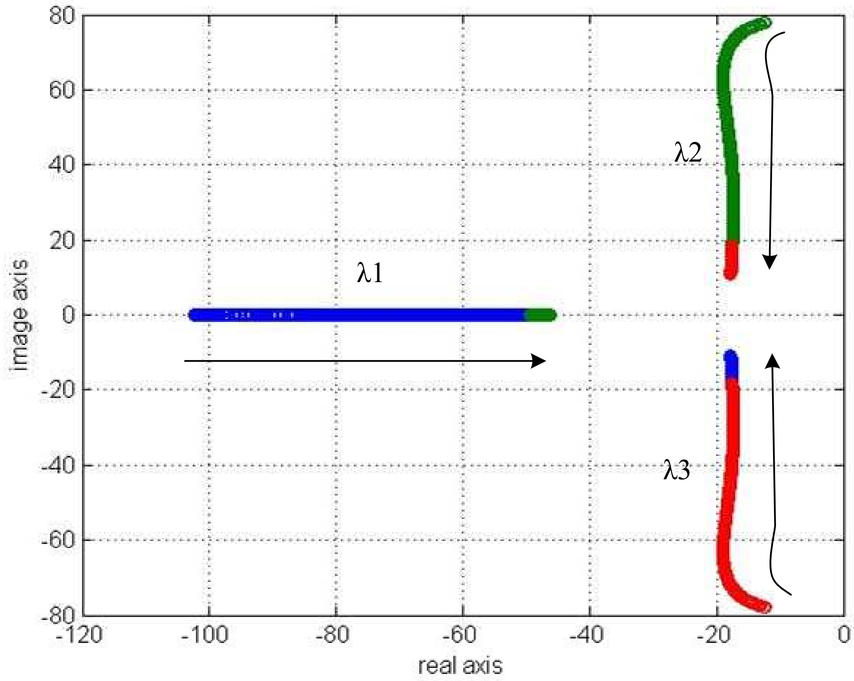

Figure 3.7: Root loci of X changes from 0.1 to 7 Ω with virtual $\omega - E$ frame control.

operating out of the preset range and may cause damage to the sensitive loads. The following sections will discuss the details of the operation range for the DG units in the virtual $\omega - E$ frame control.

3.4 Operation Range Determination

As shown in Figure 3.2, the operation range in the original $\omega - E$ frame is the rectangle determined by d (ω_{min}, E_{max}), e (ω_{max}, E_{max}), f (ω_{max}, E_{min}) and g (ω_{min}, E_{min}). When the microgrid operation is transferred from the grid-connected mode to the islanding mode, four possible variations of the power demand occurs at the PCC, as shown in Table 3.1. These four scenarios will be discussed in this section.

Table 3.1: Different power variations at PCC.

Cases	Real power	Reactive power
Case 1	Increase	Increase
Case 2	Increase	Decrease
Case 3	Decrease	Increase
Case 4	Decrease	Decrease

3.4.1 Case 1: P Increases and Q Increases

The situation in which the real power P and the reactive power Q both increase is expected to be the most common one as the microgrid should pick up as many loads as possible after a transition from the grid-connected mode to the islanding mode. This case is also the most important one as inappropriate sharing of the increased power demand might result in the damage of a DG unit. As shown in Figure 3.2, when both P and Q increase, the virtual frequency ω' and voltage E' both decrease. By using the properly defined droop range in the virtual $\omega - E$ frame, which is the shaded rectangle shown in Figure 3.2, the safe operation of the microgrid can be guaranteed. As discussed earlier, to ensure that the DG unit operates in the area represented by shaded rectangle, the droop slopes (k_p' and k_q') in the virtual frame control should be determined by using the rectangle boundary conditions for Case 1.

For the obtained virtual frame droop slopes (k_p' and k_q') from Case 1, the DG frequency and voltage operation ranges for the other three cases are discussed in the following sections.

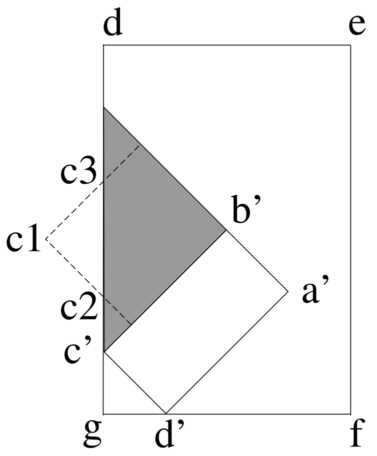

Figure 3.8: Operation range for Case 2

3.4.2 Case 2: P Increases and Q Decreases

When the real power P increases and the reactive power Q decreases, the virtual frequency ω' decreases and the virtual voltage E' increases according to the droop characteristics. This process results in the shaded operation range in Figure 3.8. In this case, a complication might occur if the desired real and reactive power sharing leads to an operation point out of the actual frequency and voltage limits, (such as c1 in Figure 3.8), and the DG operation point will be clamped to the boundary (ω_{min} in the case of Figure 3.8). For the example in Figure 3.8, the possible operation points at the left boundary are between c2 and c3, while one operation point must be determined for the DG unit.

Real or Reactive Power-Sharing Priority

At operation point c2, the real power is shared according to the predetermined slope (k_p'), and the reactive power-sharing accuracy is sacrificed due to the operation range limits. On the other hand, at the point c3, the reactive power sharing is accurate for

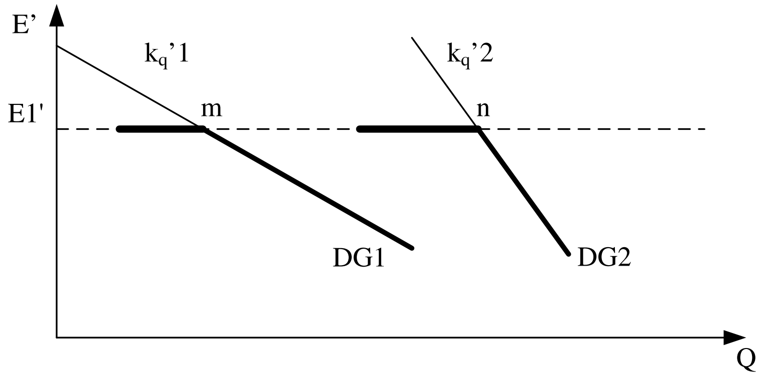

Figure 3.9: Reactive power sharing between parallel DGs

the predetermined slope (k'_q) and the real power-sharing accuracy is lost due to the operation range limits. For the operation points between c2 and c3, both the real and reactive power sharing will be affected.

For the Case 2 scenario, since the real power demand is increased, this increased demand must be accurately shared among the DG units to avoid any possible over-rating operation of the DG units. Therefore, the accurate real power sharing should be given the priority over the reactive power sharing. As a result, the DG units should preferably operate at c2.

Effect of Reactive Power Sharing

At the desired operation point c2, the virtual frequency ω' reduces to the desired value with the increase of the real power P, but the virtual voltage E' cannot further increase with the decrease of reactive Q. This problem may complicate the reactive power sharing.

Figure 3.9 shows the reactive power sharing in this situation, where the virtual voltage is clamped at $E1'$ at the point c2. In this situation, when the reactive power

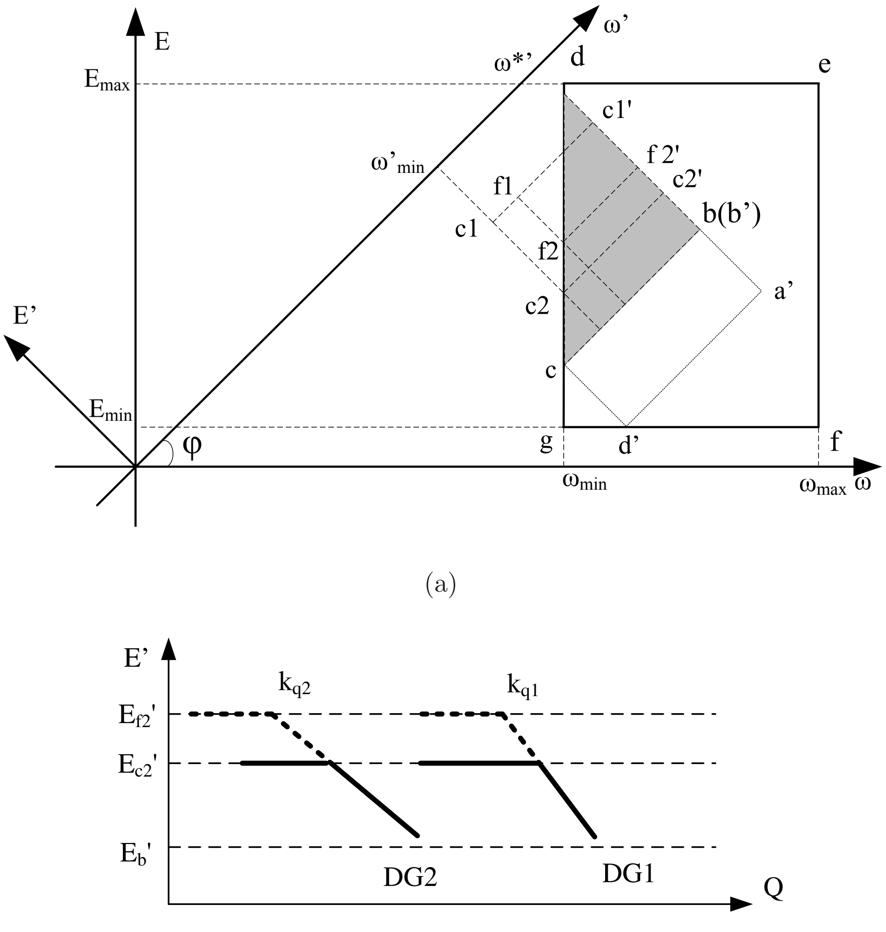

(a)

(b)

Figure 3.10: Reactive power sharing affected by real power

demand further decreases and assume that the real power demand is unchanged, the voltage cannot be over the limits $E1'$, and, therefore, the sharing of the decreased reactive power demand among the DG units will be undetermined.

The reactive power sharing accuracy is also affected by the amount of the real power demand. For example, if the increment of the total real power demand increase is reduced, the desired operation point is moved from c1 to f1, as shown in Figure 3.10(a). Consequently, the final operation point will move upward on the minimum frequency boundary from c2 to f2. This result indicates that the virtual voltage can be further increased from E'_{c2} to E'_{f2}, as shown in Figure 3.10(b), and that, therefore, the amount of undetermined reactive power-sharing will be reduced, leading to an more accurate reactive power sharing. On the other hand, if the real power demand is further increased, the reactive power sharing accuracy will be further deteriorated.

This reactive power sharing inaccuracy (due to the decrease of the Q demand) will not cause any danger to the DG units as long as the reactive power output for each DG unit is positive, as this output almost always is for the microgrid islanding operation due to the lagging power factor loads. The reactive power output is usually positive because when the total reactive power demand in a microgrid is reduced, each DG unit's reactive power output decreases according to the slope k'_q until when E' is limited as the DG unit operation is clamped to the boundary condition. Although after this point, the reduction of reactive power output will be undetermined, any increase in the reactive power output will not happen, as an increase would move the DG away from the clamped operation point.

3.4.3 Case 3: P Decreases and Q Increases

A similar analysis can be applied to the situation in which the real power P decreases and the reactive power Q increases. In this situation, the virtual frequency ω' increases and the virtual voltage E' drops. This process results in the shaded operation range shown in Figure 3.11. In this case, assuming that the desired real and reactive power sharing leads to the desired operation point of a1, and that this point is out of the actual frequency and voltage limits, the DG operation point will be clamped to the right boundary of the shaded area. Here, the boundary is determined by ω_{max}

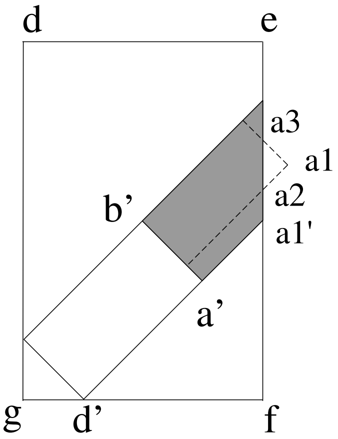

Figure 3.11: Operation range for Case 3

in the original frame.

Similarly, in this case, for the example shown in Figure 3.11, the possible operation points at the right boundary are between the points a2 and a3. At operation point a2, the reactive power is shared according to the predetermined slope (k'_q), and the real power sharing accuracy is sacrificed due to the operation range limits. Meanwhile, at the point a3, the real power is shared by the predetermined slope (k'_q), and the reactive power-sharing accuracy cannot be guaranteed. Because of the power-sharing priority, the increased demand of reactive power should have the priority to be shared accurately. Thus, the DG unit should operate at a2, where the reactive power sharing is accurate, and the real power-sharing accuracy is undetermined. Again, in Case 3, the real power demand sharing inaccuracy will not cause any danger as each DG unit will experience only a reduced real power output.

3.4.4 Case 4: P Decreases and Q Decreases

For Case 4, both the virtual frequency ω' and the virtual voltage E' will increase. The microgrid will operate safely as long as the ω' and E' variations are limited within the frequency and voltage boundary preset in the original $\omega - E$ frame, which is the rectangle determined by (ω_{min}, E_{max}), (ω_{max}, E_{max}), (ω_{max}, E_{min}) and (ω_{min}, E_{min}), as shown in Figure 3.2. For Case 4, since both the real and reactive power demands are reduced, the real and reactive power sharing will not cause problems when the DG is operated at a boundary condition. Therefore, simply limiting the output frequency and voltage should be sufficient.

Overall, the new operation ranges discussed above are practical for the virtual $\omega - E$ frame control. The use of these newly determined ranges guarantees the safe operation of the microgrid in the intentional islanding operation.

3.5 Strategy for Operation Range Control

Based on the operation range analysis in Section 3.4, the proposed strategy for the DG unit operation range control is shown in Figure 3.12, which reveals that, the real and reactive power control is achieved in the virtual $\omega - E$ frame with droop control.

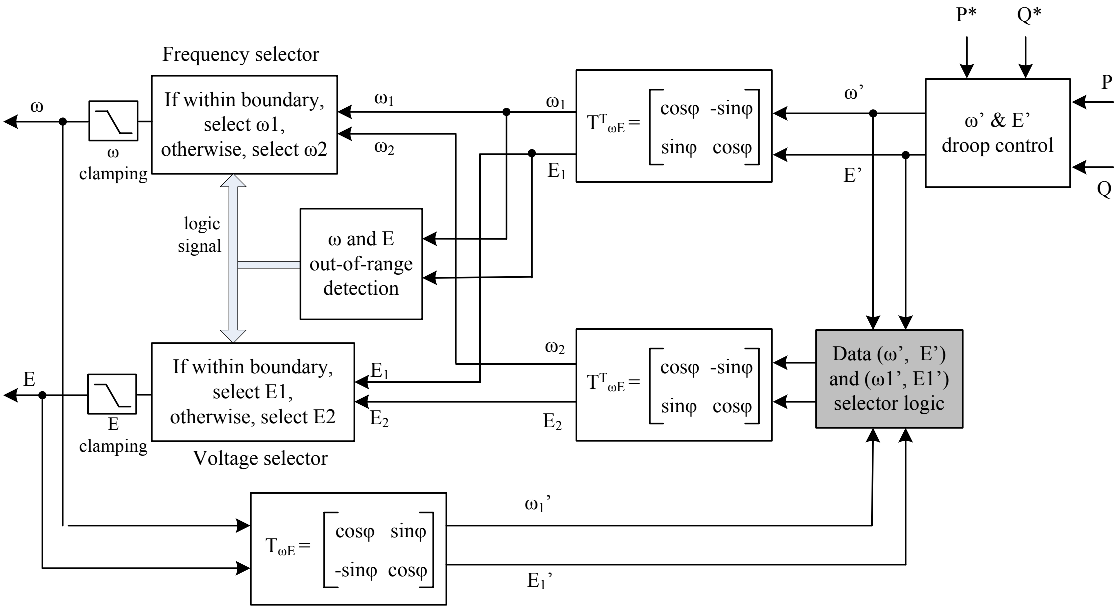

$T^{T}_{\omega E} = \begin{bmatrix} \cos\varphi & -\sin\varphi \\ \sin\varphi & \cos\varphi \end{bmatrix}$

$T_{\omega E} = \begin{bmatrix} \cos\varphi & \sin\varphi \\ -\sin\varphi & \cos\varphi \end{bmatrix}$

(a) The details of the control scheme

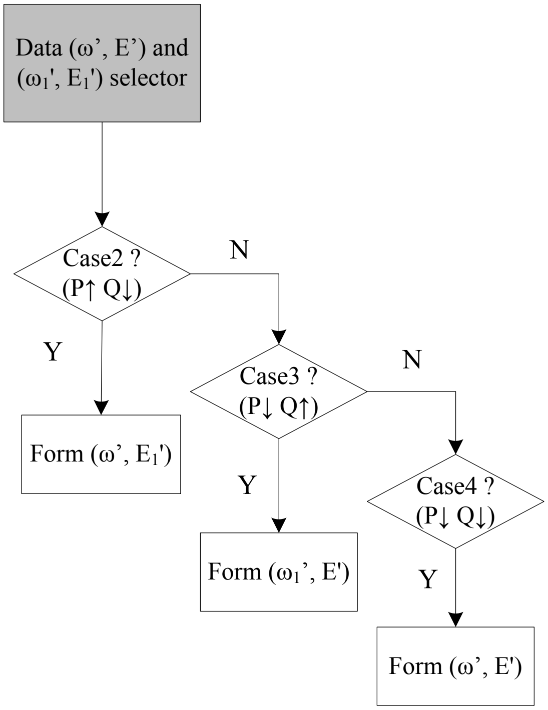

(b) The detailed logic for the data selector block

Figure 3.12: Control scheme of range determination

The outputs of the power loops are the virtual frame frequency and the voltage (ω', E'). By using the inverse transformation matrix $T_{\omega E}^{T}$, the virtual frame variables (ω', E') can be transformed back into the actual frame variables (ω_1, E_1), which are used for the operation frequency and voltage limit detection. This detection block is used to generate the control logic signal for the "Frequency selector" and "Voltage selector". If the desired operation point (determined from the droop control) is within the operation limits, the input (ω_1, E_1) of these two selectors will pass through; otherwise, input (ω_2, E_2) will pass through. Two limiters at the output of frequency and voltage selectors will clamp the operation point within the frequency and voltage limits if it is out of the boundary.

The first input to the frequency and voltage selectors (ω_1, E_1) is the desired operation point determined from the virtual frame power-sharing control, and the second input to the selectors is obtained from a feedback closed-loop control algorithm from the actual DG output (ω, E). In the feedback control, (ω_1', E_1') is the virtual frame operation point corresponding to (ω, E), and is obtained through the frame transformation. From the desired operation point and actual output operation point, a selection logic block will select the variables according to the different operation cases (discussed in the previous section), and finally (ω_2, E_2) are determined through an inverse frame transformation of the outputs of the selection logic block. The details of the selection logic block are shown in Figure 3.12(b). Basically, this operation range control scheme is implemented to ensure that the sharing priority between the real and reactive power is properly determined once an out-of-range operation occurs in the power control. To illustrate the operation of the proposed scheme, an implementation example of Case 2 scenario is explained in the following paragraphs.

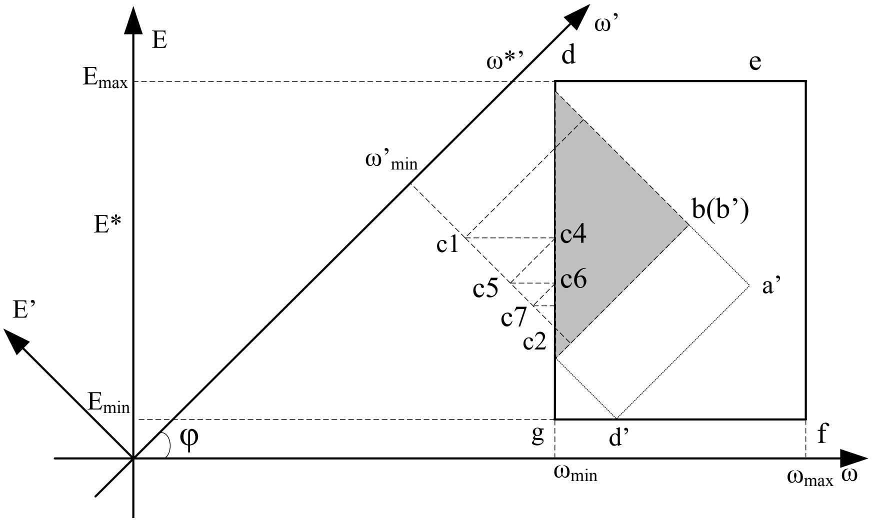

(a)

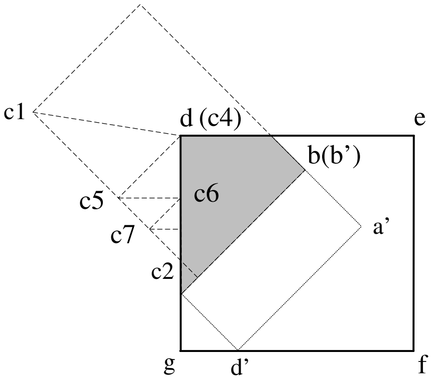

(b)

Figure 3.13: Operation point transition locus in Case 2

In Case 2, the real power increases, and the reactive power decreases, and the possible operation range for ω' and E' is the shaded area shown in Figure 3.13(a) and (b) for the two possible scenarios. As discussed previously, the desired operation point according to droop control is c1, and the DG will finally operate at the point c2 due to the boundary limitation and the priority of the accurate real power sharing.

In order to control the operation point's move from c1 to c2 in Figure 3.13(a), the operation point transition according to the proposed control strategy will be c1 → c4 → c5 → c6 → c7 → . . . → c2. This transition can be explained as it is below. The operation point of c1 is (ω_{c1}, E_{c1}) in the actual $\omega - E$ frame and (ω'_{c1}, E'_{c1}) in the virtual $\omega - E$ frame. Since ω_{c1} is less than the minimum frequency limit ω_{min}, the operation point is immediately clamped to c4 once an over range is detected. The operation point of c4 in the actual $\omega - E$ frame is (ω_{c4}, E_{c4}), where $\omega_{c4} = \omega_{min}$, and $E_{c4} = E_{c1}$. By using the transformation matrix $T_{\omega E}$, the operation point of c4 in the $\omega' - E'$ frame can be obtained as (ω'_{c4}, E'_{c4}). To move the operation point from c4 to c5, ω'_{c1} and E'_{c4} are used to make the operation point at c5 as (ω'_{c1}, E'_{c4}) in the virtual frame. The corresponding actual frame point of c5 is (ω_{c5}, E_{c5}). Once again, since ω_{c5} is less than ω_{min}, the operation point is clamped from c5 to c6. Similarly the operation point moves from c6 to c7, and eventually reaches c2, whose operation point is (ω_{c2}, E_{c2}) in the $\omega - E$ frame and (ω'_{c2}, E'_{c2}) in the $\omega' - E'$ frame, where $\omega_{c2} = \omega_{min}$ and $\omega'_{c2} = \omega'_{c1}$.

A similar operation point transition can also apply to Figure 3.13(b), where the only difference is that the over-range of the voltage is detected. For the desired operation point c1, since both the frequency and voltage are out of the limits, this point will first be clamped to point d, which is the intersection of the frequency and voltage limits. The rest part of the locus is the same as the one for Figure 3.13(a), where the operation point is moved from c4 to c2.

With the proposed control scheme, the operation point transition once an out-of-range is detected for Case 2 can be summarized as follows:

- The position on the locus from c1 to c2 has the same virtual frequency, which is the desired virtual frequency determined by the real power sharing.

- The position on the locus from c4 to c2 has the same actual frequency, which is determined by the boundary limits ω_{min}. In case of an out-of-range voltage, the corresponding actual voltage will be determined by the voltage boundary.

The achievement of the above process by using the control scheme shown in Figure 3.12 can be explained as follows: before the power demand changes, the system is operated within the defined range and (ω_1, E_1) are passed through the frequency and voltage selectors. When the real power increases leading to an actual frequency of less than ω_{min}, (ω_2, E_2) are passed through the frequency and voltage selectors. Moreover, whenever $\omega_2 < \omega_{min}$, the frequency output will be clamped to the limit ω_{min}. For the Case 2 scenario, (ω_2, E_2) are obtained from (ω', E_1'), where ω' is the virtual frequency determined from the accurate real power sharing, and E_1' corresponds to the virtual voltage once a frequency clamping occurs. Therefore (ω_2, E_2) in Figure 3.12(a) corresponds to the locus from c5 to c2 in Figure 3.13(a) and (b), and (ω, E) in Figure 3.12(a) is related to the locus from c4 to c2 in Figure 3.13(a) and (b). Obviously, the operating point will be controlled at c2 in this case.

Finally, for the virtual real and reactive power control, one can limit the virtual power operation range and make sure each DG unit is not operated beyond its real and reactive power limits. However, limiting the real and reactive power range will reduce the effective rating of the DG unit, and, as was mentioned earlier, this result is obviously not desired. Comparatively, the virtual frequency and voltage frame control will not affect the DG power ratings.

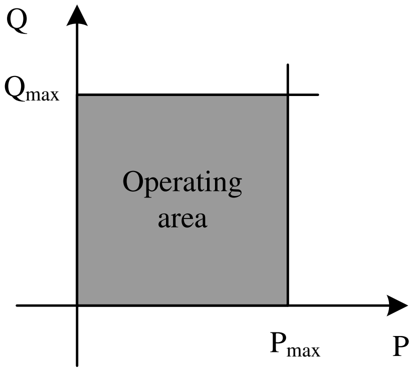

Figure 3.14: Operation capability diagram of DG unit with P_{max} and Q_{max}

3.6 Reactive Power Sharing with Adaptive Voltage Droop Control

The power control discussed so far is based on the droop method according to the fixed maximum real and reactive power ratings (P_{max} and Q_{max}) of a DG unit. Although this practice is adopted widely in the literature, the power operation range set by this method is the rectangular range shown in Figure 3.14 and does not reflect the actual DG unit capability curve.

Practically, the DG rating is defined by a maximum real power rating, which is related to the DG prime mover such as the energy from a PV cell, wind turbine, micro-turbine, etc., and a maximum apparent power rating (S_{max}) which is related to the system heating or current rating limits. The actual resulting power range of a DG unit is shown in Figure 3.15 and is similar to a synchronous generator power capability curve.

Therefore, to use the droop method for power control, the reactive power maximum limit (Q_{max}) can be adaptively obtained from the apparent power rating (S_{max})

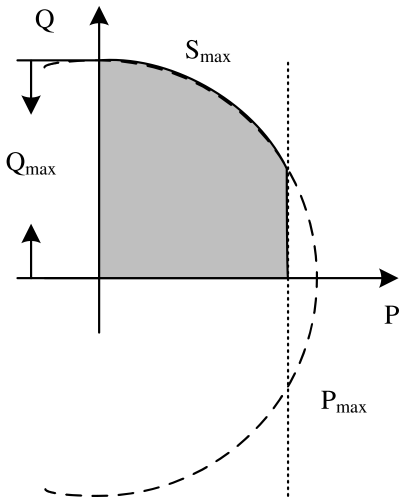

Figure 3.15: Operation capability diagram of DG unit with S_{max} and P_{max}

and the DG unit actual real power output (P) as

$$Q_{max} = \sqrt{S_{max}^2 - P^2} \tag{3.16}$$

Thus, the traditional fixed $Q-E$ droop (as presented in Chapter 2) with a fixed droop slope k_q as determined in (3.17) should be changed to the adaptive droop slope k_{q_a} as in (3.18).

$$E_{min} - E^* = -k_q(Q_{max} - Q^*) \tag{3.17}$$

$$E_{min} - E^* = -k_{q\_a}(\sqrt{S_{max}^2 - P^2} - Q^*) \tag{3.18}$$

The adaptive $Q-E$ droop characteristics are shown in Figure 3.16, which reveals that the DG terminal voltage is related to both the real and reactive power outputs. When the real power output is zero, $Q_{max} = S_{max}$, and the droop slope (> 0) has the smallest value. When the real power increases, Q_{max} is reduced adaptively, and the droop slopes increases to ensure a DG unit operation range as shown in Figure 3.15.

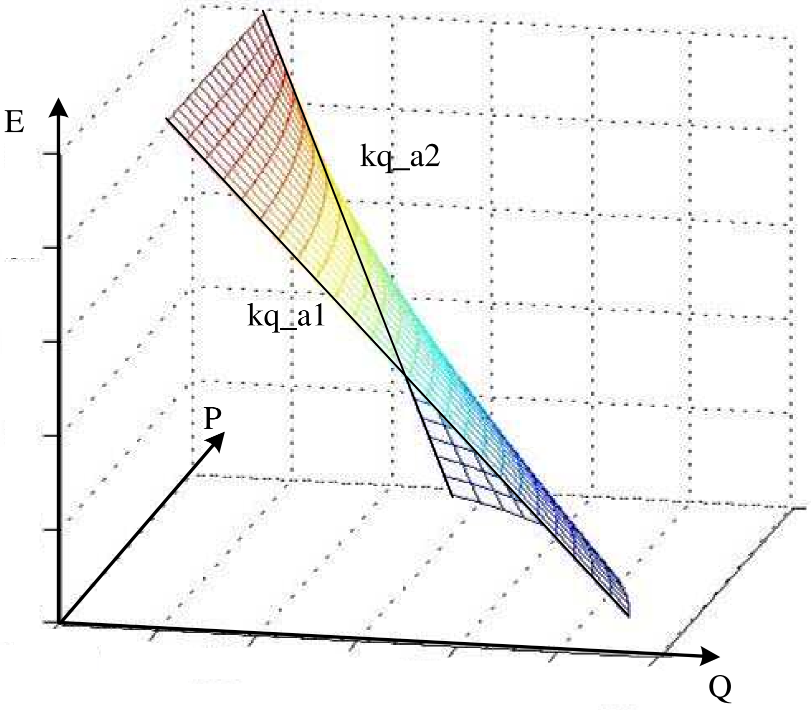

Figure 3.16: Adaptive voltage droop characteristics

This adaptive droop control of reactive power can also improve the system stability because when the fixed Q_{max} is used as in the traditional droop control, this reactive power limit needs to be the maximum possible reactive power when the real power is also at maximum to guarantee that an over current does not occur. With the adaptive droop control, with the decrease of the output real power, Q_{max} increases adaptively. This leads to a reduced droop slope and therefore improves the system stability.

By performing a small signal model analysis, the system stability can be investigated by using the root locus plot shown in Figure 3.17. This figure reveals that with the decrease in the droop slope k_{q_a}, which is associated with the adaptive $Q - E$ droop control, the pair of complex-conjugate dominant roots $\lambda 2$ and $\lambda 3$ move left

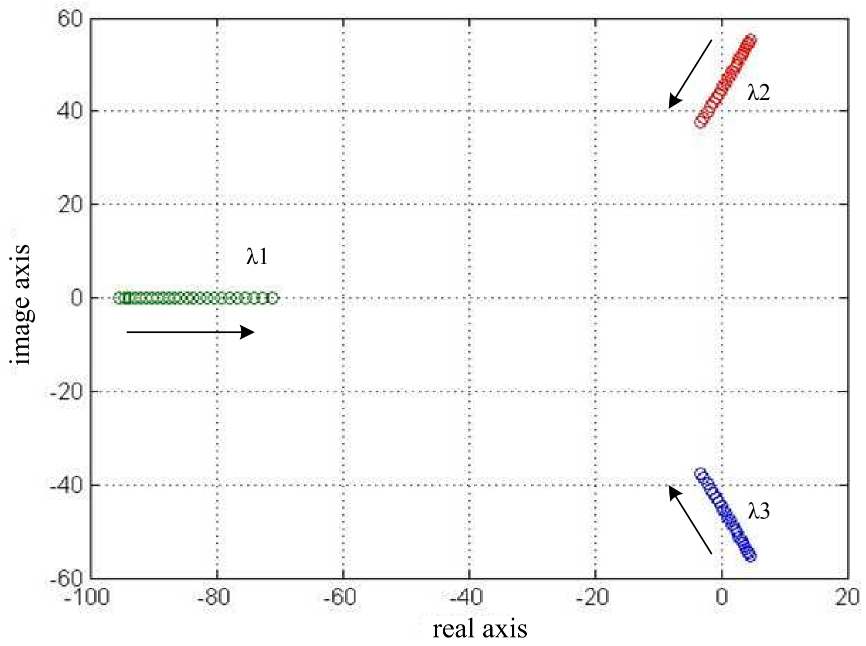

Figure 3.17: System root loci as k_{q_a} decreases (with $R/X = 10/1$)

toward the more stable region. In other words, the system has better stability with the decrease in the droop slope. By using a mainly inductive impedance, the system stability can be maintained with variation of k_q as shown in Figure 2.7, however, a reduction of k_q can still improve the damping of the system.

This adaptive reactive power control will adjust only the Q_{max} and therefore the $Q - E$ droop slope (k_{q_a}). This adjustment will not affect the actual DG unit capability curve and the preset DG unit frequency and voltage operation range. Similarly, at the virtual frequency and voltage frame, the operation range will not be affected, and only the droop slope (k'_{q_a}) will be adjusted adaptively. As a result, the operation of the virtual frame power control and the operation range control strategy as discussed previously, will not be affected.

3.7 Summary

In this chapter, a modified droop control method based on virtual frequency and voltage frame transformation was proposed. This method effectively decoupled the real and reactive power control and improved the system stability, which were verified by a small signal analysis. Furthermore, to guarantee the safe operation of DG units and sensitive loads, a thorough analysis of the virtual frame operation range and its relationship to the actual operation limits was conducted. A control strategy for automatic range determination based on a closed-loop algorithm was also proposed. Finally, a reactive power control based on an adaptive voltage droop was proposed. This control method can enlarge the power output range and further improve the system stability. Simulation and experimental results are provided in the next chapter to verify the performance of the proposed power control scheme.

Chapter 4

Simulation and Experimental Verifications

To verify the stability analysis conducted in the previous chapters and test the performance of the proposed virtual frequency and voltage frame power control scheme, both computer simulation and experimental results from a 5 kVA microgrid prototype are obtained. In the simulations and experiments, a microgrid system with two inverter based DG units as illustrated in Figure 4.1 is considered. The two DG units in the microgrid are designed to have the same parameters. Also, the same system parameters are used for both the simulations and the experiments are shown in Table 4.1.

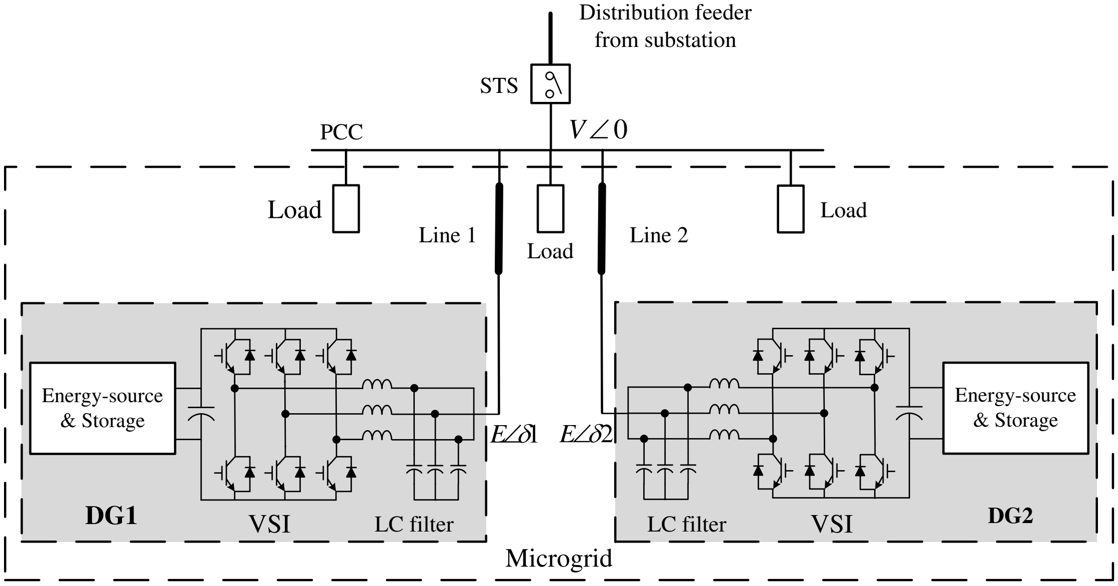

Figure 4.1: A microgrid with two power electronics based DG system

4.1 Simulation Results

MATLAB/Simulink is employed for the simulations. A discrete model is built in this simulation with sampling time $Ts = 5 * 10^{-5}$ s. This model contains two parts: the control and physical elements of the system. The control part is built with the control schemes shown in Figure 2.1 and Figure 3.5, which are the traditional droop control and virtual $\omega - E$ control schemes, respectively. The multiple P+ resonant controller is modeled by using the s-domain functions presented in equation (2.1). The traditional droop controller and the one modified with virtual $\omega - E$ frame transformation are modeled by the equations presented in Chapter 2 and Chapter 3, respectively. The SimPowerSystems library of Simulink is used to model the electrical system components in Figure 4.1. Since only the islanding operation mode

Table 4.1: Simulation and experiment parameters

	Parameters	Values
DG systems	Inverter switching frequency	4.5 kHz
	Inverter filter inductance	5 mH
	Inverter filter capacitance	40 μF
	DC-link voltage	230 V
Controller parameters for each DG unit	ω^*	$60 \times 2\pi$ rad/s
	ω_{min}	$59.5 \times 2\pi$ rad/s
	E^*	85 V
	E_{min}	80 V
	P^*	175 W
	P_{max}	500 W
	Q^*	75 Var
	Q_{max}	225 Var
	Line impedance (Z)	1 Ω

is considered, the main SimPowerSystems elements used in the system model are the ideal DC voltage source, VSI, inductors, capacitors, $3-\phi$ series RLC branches, and $3-\phi$ series RLC load. The VSI model uses a universal bridge to model the three-phase power converter consisting of six power switches connected in a bridge configuration and using IGBT/Diodes for the switching devices. This converter is driven by a gating signal coming from the PWM block.

Since the two DG units have the identical parameters, only the real and reactive power outputs of DG1 are shown here.

4.1.1 Stability Investigation

The first set of simulations is for the system stability investigation with the traditional droop control and the proposed virtual frame droop control. A RL load with 540 W and 270 Var is connected at the PCC, and the line impedance for both DG units is $Z = 1\Omega$ with varying impedance angle. The interfacing inverters are operated with a switching frequency of 4.5 kHz. In the simulations, the microgrid is started with the proposed virtual frame control of each DG unit, and the control scheme for each DG unit is switched to the traditional control at the actual $\omega - E$ frame at $t = 0.6$ s.

Figure 4.2 shows the control performance with mainly inductive line impedance, where the R/X ratio is 1/10. Obviously, the system stability is maintained under both control schemes due to the mainly inductive line impedances. The slight drops of both the real and reactive power when the control scheme is switched to the actual $\omega - E$ frame are due to the $\omega - E$ operation range differences shown in Figure 3.2, and result in slightly lower operation voltages for DG systems.

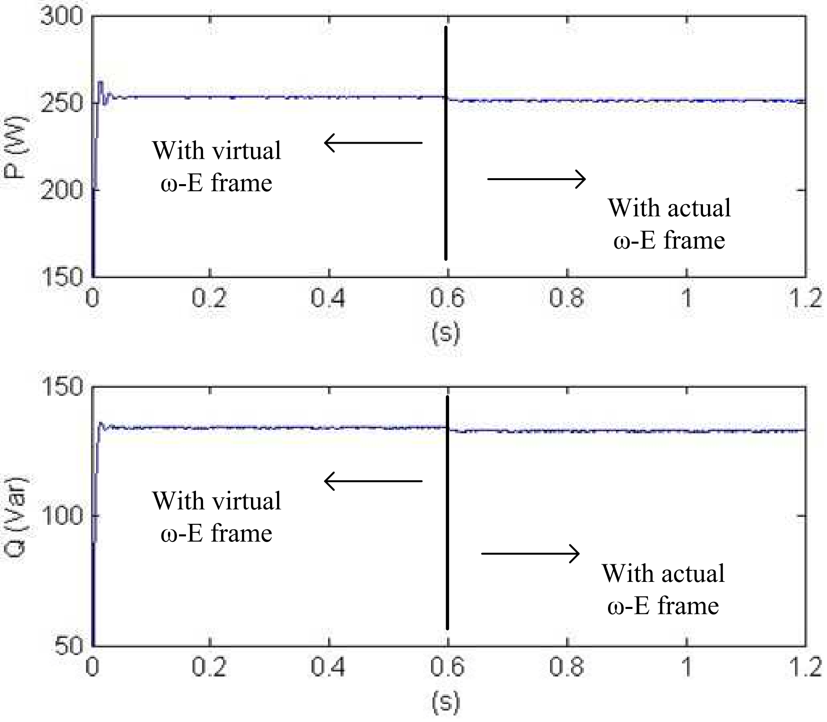

Figure 4.2: Real and reactive power outputs of DG 1 with inductive impedance (the virtual frame control is switched to actual frame control at $t = 0.6s$)

The scenario of a microgrid with mainly resistive line impedance with a R/X ratio of 10/1 is shown in Figure 4.3. As expected, the proposed virtual $\omega - E$ frame control guarantees the microgrid stability and, at the same time, directly controls the real and reactive power sharing. Figure 4.3 reveals that the DG1 output real and reactive powers are half of the total PCC load demands due to the same DG unit parameters selected. When the traditional $\omega - E$ frame control is used, the system stability is lost, and this result is consistent with the small signal analysis results shown in Chapter 2.

Figure 4.4 shows the situation of a microgrid with both resistive and inductive

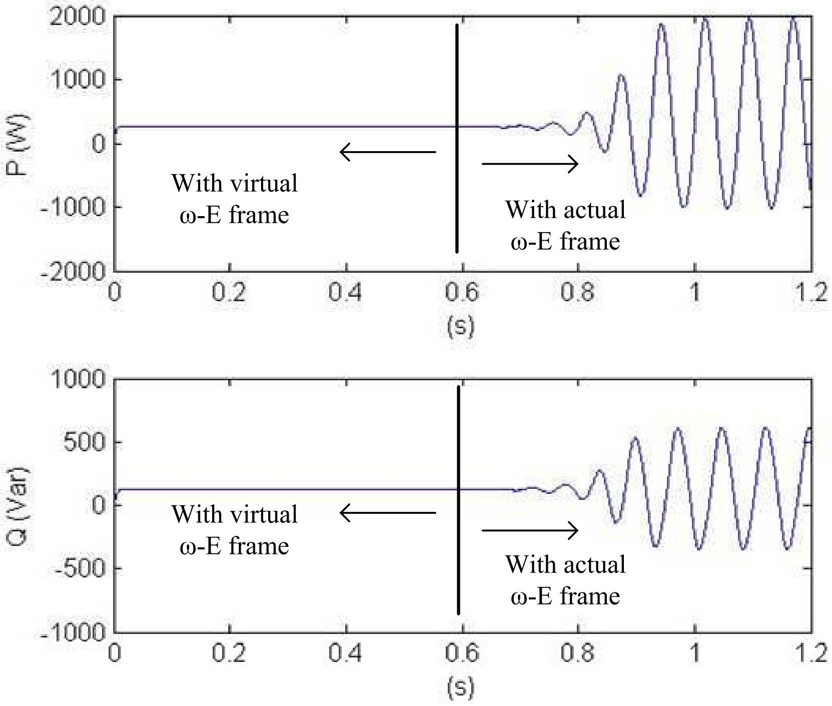

Figure 4.3: Real and reactive power outputs of DG 1 with resistive impedance (the virtual frame control is switched to actual frame control at $t = 0.6s$)

impedances (for DG1 and for DG2). Once again, the proposed virtual frame control shows a superior performance with improved system stability compared to that of the traditional droop method in the actual $\omega - E$ frame.

4.1.2 Range Determination in The Virtual $\omega - E$ Frame

Figure 4.5 shows the simulation results from a frequency and voltage transition in the operation range control process under the Case 2 scenario ($P \uparrow Q \downarrow$). In this simulation, to create an out-of-range operation condition, the maximum real and reactive power limits for both DG units are set to 350 W and 150 Var, respectively, and the microgrid is operated with a PCC load transition from 300 W and 110 Var

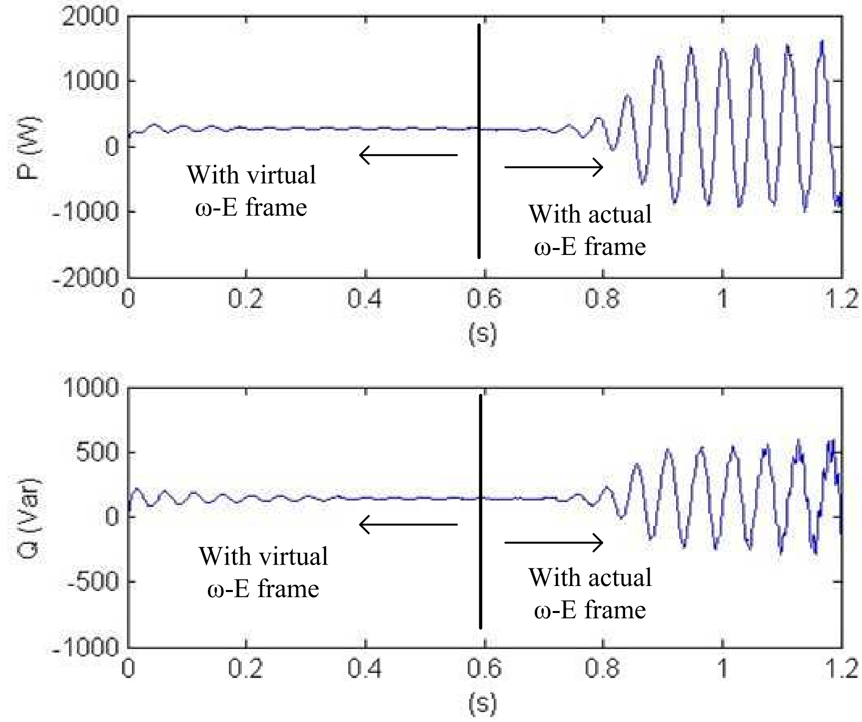

Figure 4.4: *PQ* outputs of DG 1 with combination of resistive and inductive impedances (the virtual frame control is switched to actual frame control at $t = 0.6s$)

to 640 W and 40 Var, respectively.

The operation points of DG1 under this simulation are shown in Figure 4.5, where Figure 4.5(a) shows the operation point transition at the actual frequency and voltage frame, and Figure 4.5(b) presents the zoomed-in view of Figure 4.5(a) at the frequency boundary. Figure 4.5(a) clearly reveals the original operation point before the load transient, and the desired operation point according to droop control after the transition. The desired operation point according to droop control is obviously at the left of the minimum frequency limit. The circled part of Figure 4.5(a) is the actual operation point transition locus achieved with the proposed range control scheme.

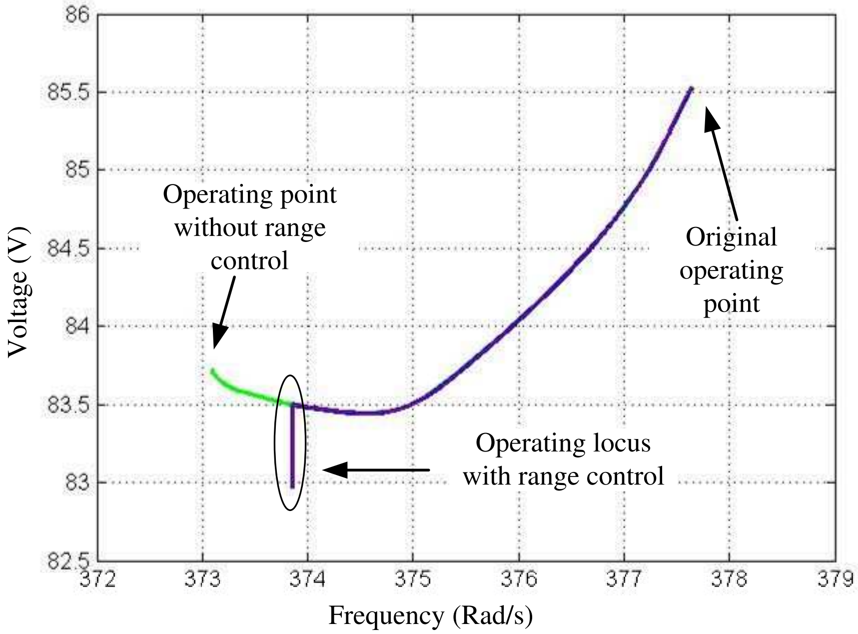

(a) Full transition plot

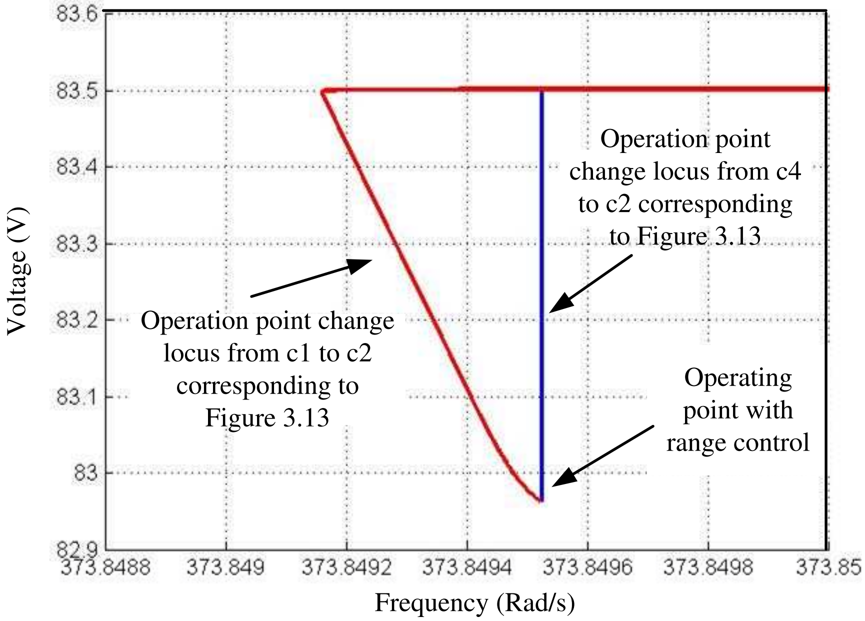

(b) Zoomed-in view of range limitation part

Figure 4.5: Operation point transition of DG 1 in Case 2 scenario.

A zoomed-in view of the operation point transition is shown in Figure 4.5(b). This view is consistent with the results in Figure 3.13(a). The only difference is that c1 in Figure 3.13(a) is the desired operation point from the droop control, and is the same as the operation point without range control in Figure 4.5(a), while in Figure 4.5(b), the point corresponding to c1 is where an out-of-range is first detected in the control algorithm, and is much more closer to the minimum frequency limit. Obviously, the DG unit will operate at the frequency boundary and with accurate real power sharing.

4.1.3 Adaptive Voltage Droop Control

The last simulation is run to verify the improvement of stability when the adaptive reactive power droop control is implemented. With the simulation parameters in Table 4.1, it can be obtained that $S_{max} = \sqrt{P_{max}^2 + Q_{max}^2} = 550$ VA. Figure 4.6 shows the real and reactive power outputs of DG 1 with the system using the adaptive $Q - E$ droop slope k'_{q_a}, and the control scheme changed from the virtual $\omega - E$ frame to the actual $\omega - E$ frame. Figure 4.6(a) shows the control performance with mainly inductive line impedance, where the R/X ratio is 1/10, and Figure 4.6(b) shows the system with mainly resistive line impedance with R/X ratio of 10/1. The system stability is maintained even with the traditional droop control under the resistive line impedances. Obviously, compared to the results shown in Figure 4.3, this improvement of stability is due to the adaptive reactive power droop control, which uses a smaller voltage droop slope.

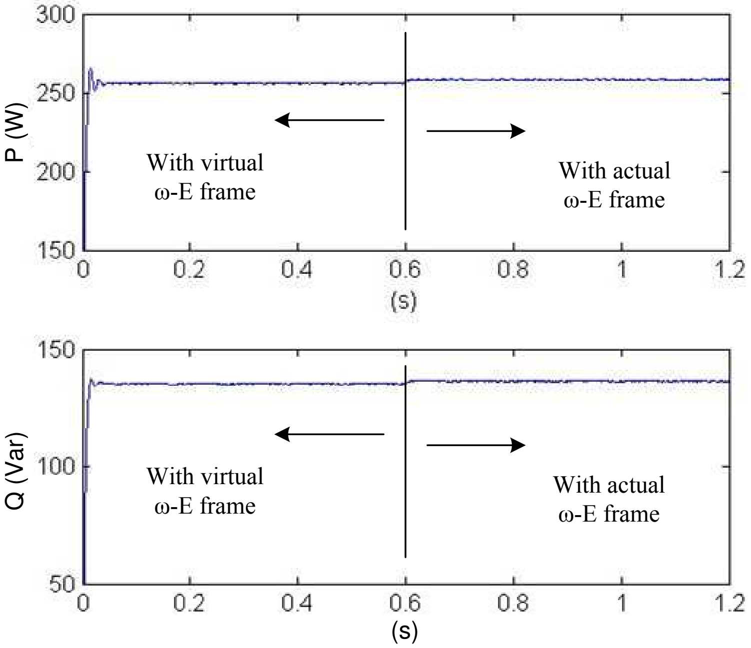

(a) With inductive impedance

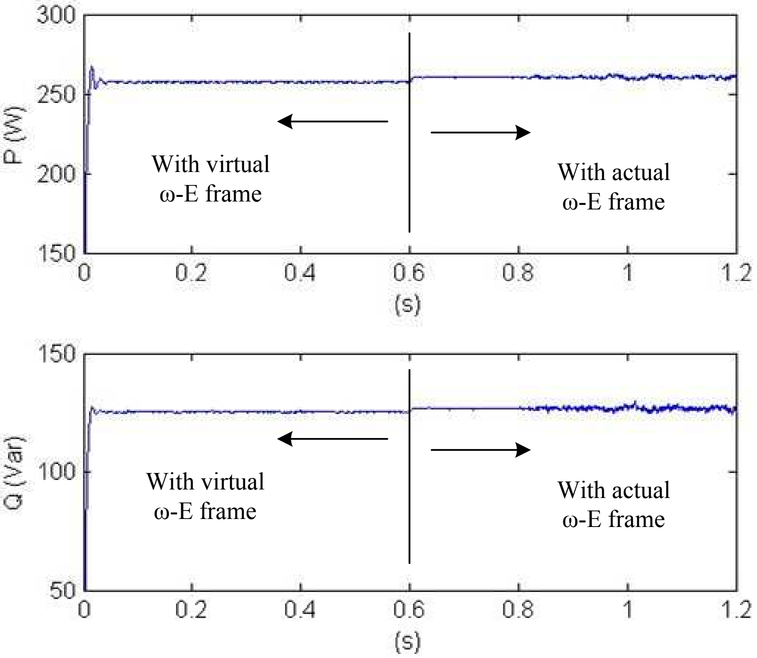

(b) With resistive impedance

Figure 4.6: Real and reactive power outputs of DG 1 with adaptive $Q - E$ droop slope (the virtual frame control is switched to actual frame control at $t = 0.6$ s).

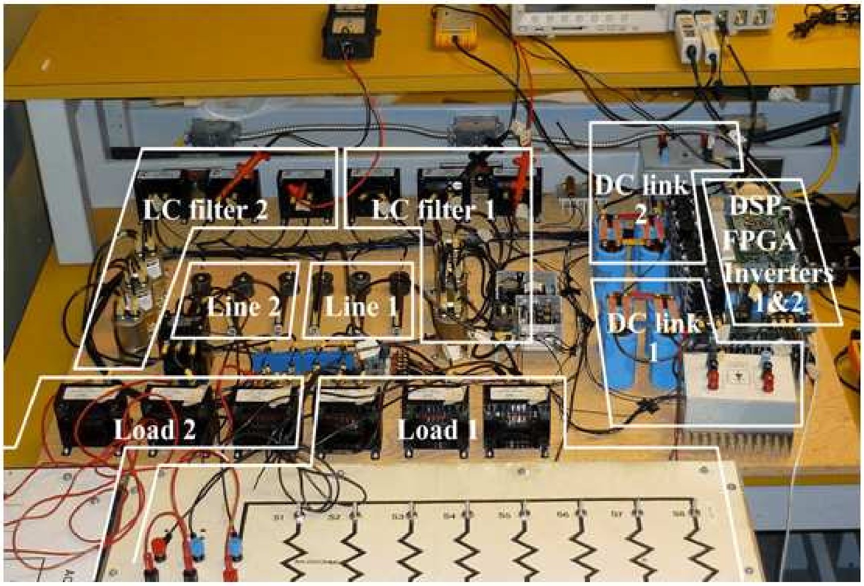

Figure 4.7: Experimental microgrid prototype with two DG systems.

4.2 Experimental Results

A hardware microgrid with two DG systems as shown in Figure 4.1 is also constructed for experimental verification of the proposed control strategy. The hardware microgrid system parameters are designed to be the same as those in the simulation model and are shown in Table 4.1. In the experiment, each DG system contains a dc link at 230V, a three-phase voltage source interfacing inverter and a LC output filter. The two DG systems are controlled with a DSP-FPGA control system, where the TMS-F2812 DSP is programmed with the proposed power control algorithms and the FPGA is used for the space vector pulse-width modulation (SVPWM) signal generation and system protection. A picture of the microgrid system is shown in Figure 4.7. In the experiment, two loads are connected in parallel at the PCC, with a total load demand of 540W and 270Var. The resistive line impedance between each DG units and the PCC is $Z = 1 + j0.09\Omega$, with the R/X ratio of 11/1.

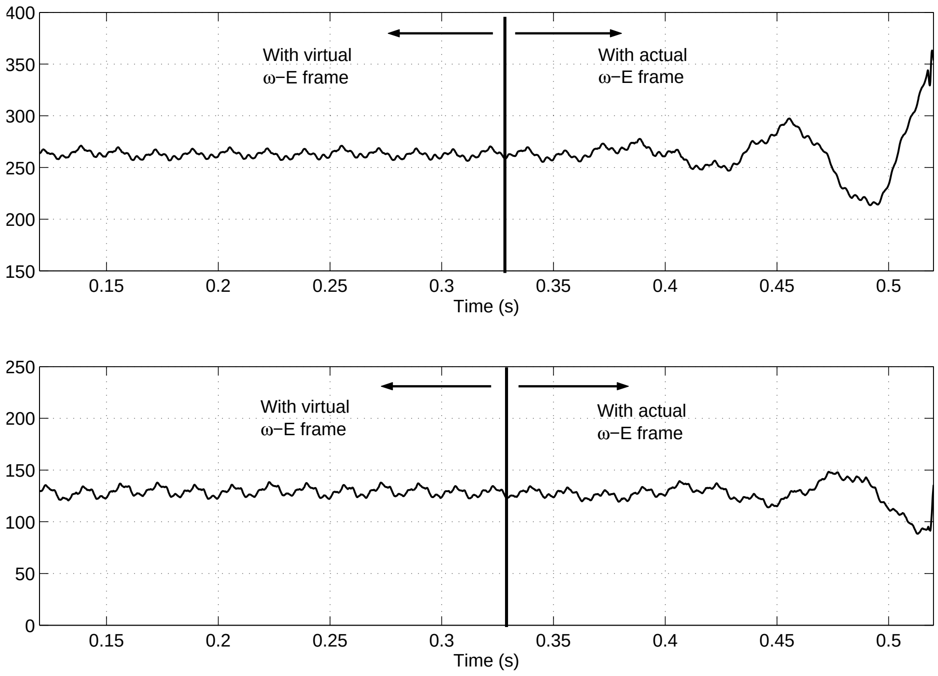

Figure 4.8: Real and reactive power outputs of DG 1 with resistive impedance (the virtual frame control is switched to actual frame control at t=0.33s).

4.2.1 Stability Investigation

The first experiment is for system stability investigation. In this experiment, the microgrid is initially operated with the virtual $\omega - E$ frame control and the control scheme of each DG is switched to the traditional $\omega - E$ frame control at $t = 0.33$s. The real and reactive power outputs of DG 1 are shown in Figure 4.8. As expected, with the mainly resistive line impedances, the proposed virtual $\omega - E$ frame control guarantees the microgrid stability and controls/shares the real and reactive power equally between the two DG systems (with the same parameters selected), while when the traditional $\omega - E$ frame control is used, the DG systems become unstable

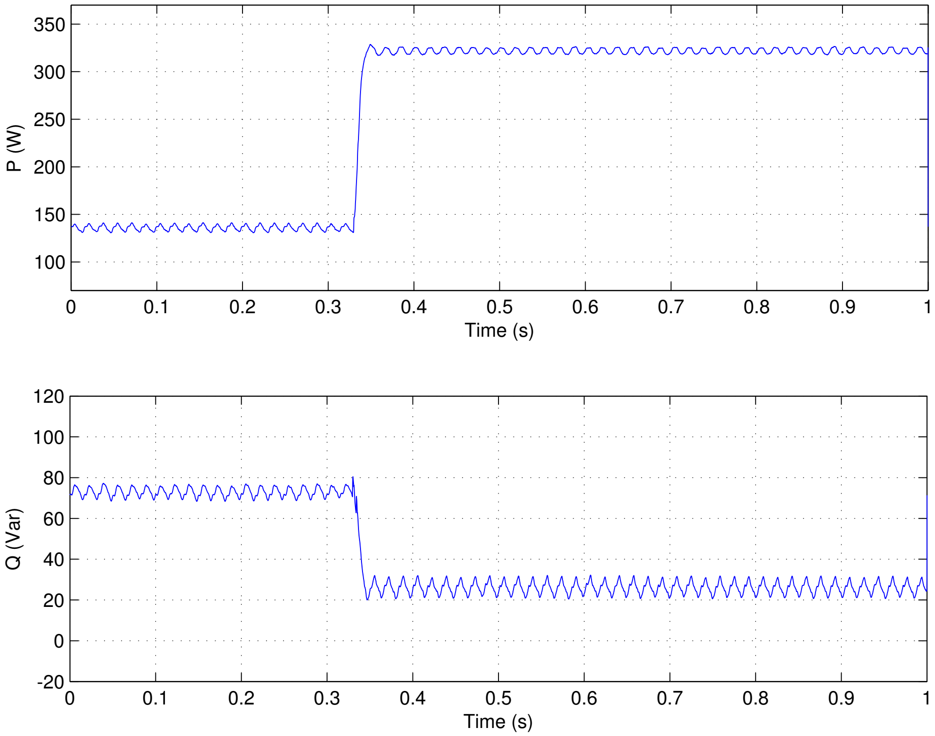

Figure 4.9: PQ outputs of DG 1 under microgrid load transition (Case 2 scenario).

as illustrated in Figure 4.8.

4.2.2 Range Determination in The Virtual $\omega - E$ frame

The second experiment is run for the verification of the proposed operation range control strategy. Similar to the DG power limits in the simulations, the DG power limits are adjusted ($P_{max} = 350W$ and $Q_{max} = 150W$), and a Case 2 type microgrid load transition is introduced so that each DG will experience an output power transition from 135 W and 75 Var to 320 W and 20 Var at $t = 0.3s$ as shown in Figure 4.9. With this power demand transition, an out-of-range situation will be created. The DG1 operation point transition is shown in Figure 4.10 (a) and (b).

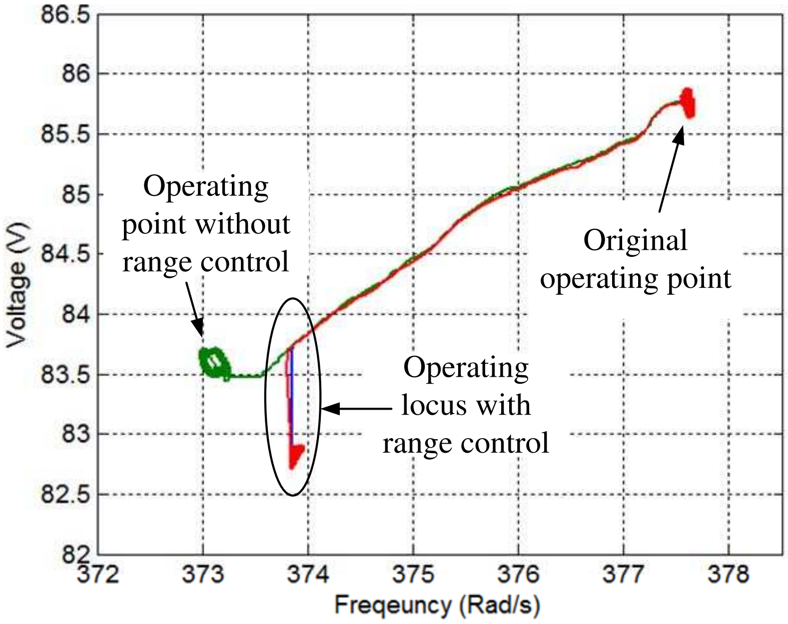

(a) Full transition plot

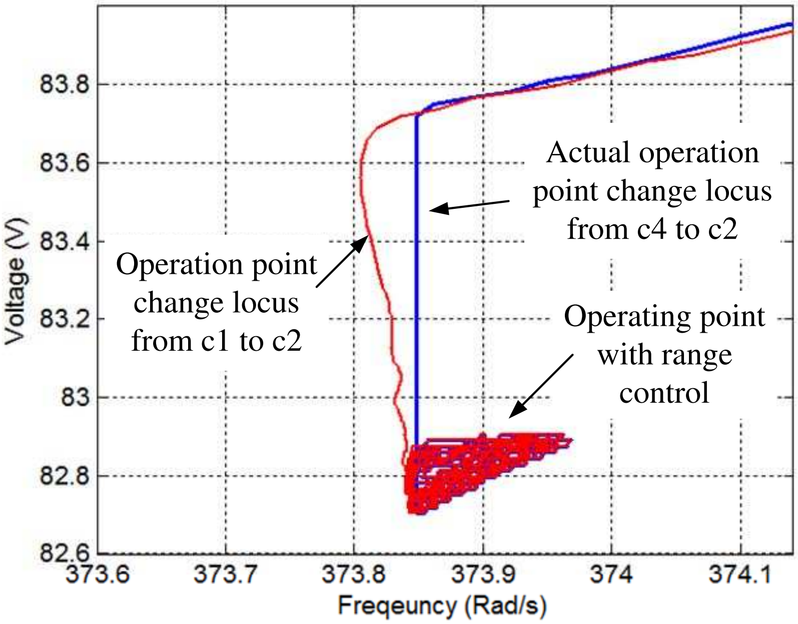

(b) Zoomed-in view of range limitation part

Figure 4.10: Operation point transition of Case 2 scenario.

As expected, without the range control, the DG system will operate at a frequency lower than the minimum limit, as shown in Figure 4.10(a), while with the implementation of the proposed control strategy, the operation point will move along the frequency boundary for accurate real power sharing due to the real power sharing priority for the Case 2 scenario.

The zoomed-in view of the operation point transition is consistent with the results shown in Figure 4.10, where the locus from c5 to c2 and from c4 to c2 is clearly shown in Figure 4.10(b). Similar to the simulation results shown in Figure 4.5(b), the locus of ($\omega 2$, $E2$) starts to move toward c2 immediately after an over-range is detected in the control algorithm, and, therefore, this locus is quite close to the minimum frequency boundary. The enlarged steady state operation point as shown in Figure 4.10 (a) and (b) is due to the non-perfect frequency and voltage in the microgrid system (the power oscillations will introduce very slight frequency and voltage oscillations through the droop control).

4.3 Summary

Simulations using Matlab/Simulink and experiments on a hardware microgrid prototype were conducted in this chapter to test the effectiveness and performance of the proposed virtual frequency and voltage frame power control strategy. The same parameters were selected for both the simulations and the experiments, and the obtained results from the two tests matched. From these simulations and experiments, it can be verified that the dynamics and stability of the microgrid system was improved with the proposed virtual frame control strategy. In a low-voltage microgrid with resistive line impedance, the virtual frame control can guarantee the system stability. Moreover, the control algorithms for controlling the DG units to operate within the preset voltage and frequency range were tested, and the measured DG operation loci verified the control method's effectiveness. The proposed adaptive voltage droop control method using the practical DG compatibility curve was also tested in this chapter, and the results verified this method's improved stability.

Chapter 5

Conclusion and Future Work

The rapidly increasing energy demand is becoming a growing concern for most countries. To deal with the increasing energy demand, the attempt to develop renewable energy will be a main trend in the future. Distributed energy resources such as wind, PVs, fuel cells, and micro-turbines have been used to provide an alternative to or an enhancement of the traditional electric power system. The microgrid concept based on power electronics inverters is very effective in integrating the distributed energy resources for providing electric power with high quality and high reliability. A key feature of a microgrid is its ability during a utility-grid disturbance to separate and isolate itself from the utility seamlessly with little or no disruption to the loads within the microgrid. Then, when the utility grid returns to its normal condition, the microgrid can resynchronize and reconnect itself to the grid, in an equally seamless fashion [48]. The proper operation of a microgrid should enable it to function as a safe and reliable network, but requires the development of some new innovations including those for a control strategy and a protection scheme. One of the most critical issues, power control strategy, was addressed in this thesis.

In the islanding operation of a microgrid, its DG units are governed by droop control algorithms so they can operate with enhanced reliability in a de-centralized fashion without any communication. The droop controls allow the DG units to come in and out of the system at the level of “plug-and-play” flexibility depending on their availability and the demand of the loads. The conventional real power-frequency droop control and the reactive power-voltage droop are most effective if the transmission line is inductive. However, the microgrid is usually in the distributed network at a low-voltage level, so that the line impedance can be either resistive (with a directly connected DG) or inductive (with a DG with a coupling transformer or inductor) compared to its transmission system counterpart. Thus, the traditional droop control will cause power flow coupling and microgrid system stability concerns. Some approaches have been proposed to address this issue. For example, a virtual real and reactive power frame transformation has been proposed to modify the droop control method by taking the transmission line impedance ratio into account. However, this method cannot guarantee real and reactive power sharing accuracy and will cause the inefficient use of DG units due to the inconsistency between the DG ratings and actual output power range. Inspired by this virtual power frame control method, we proposed a novel virtual frequency and voltage frame control strategy, which can effectively decouple the real and reactive power flows and improve the system transient and stability performance. Thus, this thesis focused on the development, analysis, simulation, and experimental verification of the proposed power management strategy.

5.1 Thesis Contributions

This thesis proposed a virtual frequency and voltage frame droop method for power sharing and control among the DG units in a low-voltage power electronics-based microgrid in the islanding operation mode. The proposed frame transformation method effectively addressed the problems associated with the traditional frequency and voltage droop control by decoupling the real and reactive power control and improving the microgrid system stability. This frame transformation was achieved by rotating the actual frequency and voltage ($\omega - E$) frame into a virtual frequency and voltage ($\omega' - E'$) frame. Thus, the power flow relationship was decoupled by changing from $P - \omega$ and $Q - E$ droop control to $P - \omega'$ and $Q - E'$ droop control.

A small signal model analysis was carried out to investigate the microgrid system stability under different control methods. According to the developed small signal model, root locus analyses were conducted and showed that under the traditional droop control the system had better stability with inductive line impedance, while the system became less stable or even unstable with resistive line impedance. When the proposed virtual frequency and voltage frame power control method was implemented with a frame transformation angle of $\varphi = 45°$, the system stability was maintained for either mainly resistive or mainly inductive line impedance. Thus, it was shown that the proposed virtual frequency and voltage frame droop method guaranteed the system stability in a low-voltage microgrid.

Moreover, a proper operation range determination control strategy for the virtual frequency and voltage frame was also proposed, which guaranteed that each DG unit would operate in the predefined frequency and voltage variation range in the virtual frame to maintain superior power quality. Furthermore, an adaptive reactive power droop method was proposed, which features an enlarged power output range compared to that of the traditional droop control and further improved system stability. Finally, simulation and experimental results were obtained to demonstrate the effectiveness of the proposed power control strategy.

The proposed control method could also be used for a microgrid with both power electronics-based DG systems and rotational machine-based DG systems. In such a microgrid, the machine-based DG systems could be controlled with their desired power outputs and considered as a part of the load, so the power electronics-based DG systems could share the remaining power demands with the virtual voltage and frequency control. Moreover, the virtual frame control could also be implemented for the parallel operation of power electronics-based uninterruptable power supply (UPS) systems, where the total load real and reactive power demands need to be shared properly according to the rating of each UPS system.

5.2 Future Work

This thesis provided a novel power control method for a low-voltage power electronics-based microgrid in the autonomous operation mode. The recommendations for future work on this topic are summarized below:

- As discussed earlier, the control method is also applicable to a microgrid with both electronics interfaced DG units and non electronics interfaced DG units, such as diesel generators. However, simulations and experiments on such a hybrid microgrid need to be conducted to investigate the system performance and indentify any possible complications.

- The power control strategy was developed based on an autonomous microgrid. Similarly, in the grid-connected operation, power flow coupling still exists due to the resistive low-voltage distribution feeders. However, since the grid frequency and voltage magnitude can be assumed to be constant in the grid-connected operation, direct implementation of the virtual frame control in the grid-connected mode might not be possible. Therefore, the development of a power control strategy for grid-connected operation based on the power decoupling concept proposed in this thesis is another recommended research direction.

Bibliography

[1] M. S. S. J. D. Glover and T. J. Overbye, *Power system analysis and design.* Thomson Corportation, 2008.

[2] G. M. Masters, *Renewable and Efficient Electric Power Systems.* John Wiley & Sons, 2004.

[3] J. Carrasco, L. Franquelo, J. Bialasiewicz, E. Galvan, R. Guisado, M. Prats, J. Leon, and N. Moreno-Alfonso, "Power-electronic systems for the grid integration of renewable energy sources: A survey," *Industrial Electronics, IEEE Transactions on*, vol. 53, pp. 1002–1016, June 2006.

[4] M. R. Patel, *Wind and solar power system: Design, Analysis and Operation.* CRC Press, Taylor & Francis Group, 2006.

[5] "World wind energy association." Available: http://www.wwindea.org/home/index.php.

[6] M. Liserre, R. Teodorescu, and F. Blaabjerg, "Stability of photovoltaic and wind turbine grid-connected inverters for a large set of grid impedance values," *Power Electronics, IEEE Transactions on*, vol. 21, pp. 263–272, Jan. 2006.

[7] F. Blaabjerg, Z. Chen, and S. Kjaer, "Power electronics as efficient interface in dispersed power generation systems," *Power Electronics, IEEE Transactions on*, vol. 19, pp. 1184–1194, Sept. 2004.

[8] D. Georgakis, S. Papathanassiou, N. Hatziargyriou, A. Engler, and C. Hardt, "Operation of a prototype microgrid system based on micro-sources quipped with fast-acting power electronics interfaces," in *Power Electronics Specialists Conference, 2004. PESC 04. 2004 IEEE 35th Annual*, vol. 4, pp. 2521–2526 Vol.4, 2004.

[9] P. Dahono, A. Purwadi, and Qamaruzzaman, "An lc filter design method for single-phase pwm inverters," in *Power Electronics and Drive Systems, 1995., Proceedings of 1995 International Conference on*, pp. 571–576 vol.2, Feb 1995.

[10] T. Kawabata, T. Miyashita, and Y. Yamamoto, "Digital control of three phase pwm inverter with l-c filter," in *Power Electronics Specialists Conference, 1988. PESC '88 Record., 19th Annual IEEE*, pp. 634–643 vol.2, April 1988.

[11] G. Andersen, C. Klumpner, S. Kjaer, and F. Blaabjerg, "A new green power inverter for fuel cells," in *Power Electronics Specialists Conference, 2002.PESC' 02. 2002 IEEE 33rd Annual*, vol. 2, pp. 727–733 vol.2, 2002.

[12] R. Lasseter, "Microgrids," in *Power Engineering Society Winter Meeting, 2002. IEEE*, vol. 1, pp. 305–308 vol.1, 2002.

[13] R. H. Lasseter, "Microgrids and distributed generation," *Journal of Energy Engineering, American Society of Civil Engineers*, Sept. 2007.

[14] M. Barnes, J. Kondoh, H. Asano, J. Oyarzabal, G. Ventakaramanan, R. Lasseter, N. Hatziargyriou, and T. Green, "Real-world microgrids–an overview," in *System of Systems Engineering, 2007. SoSE '07. IEEE International Conference on*, pp. 1–8, April 2007.

[15] R. Lasseter and P. Piagi, "Providing premium power through distributed resources," in *System Sciences, 2000. Proceedings of the 33rd Annual Hawaii International Conference on*, pp. 9 pp.–, Jan. 2000.

[16] Y. W. Li, D. Vilathgamuwa, and P. C. Loh, "Design, analysis, and real-time testing of a controller for multibus microgrid system," *Power Electronics, IEEE Transactions on*, vol. 19, pp. 1195–1204, Sept. 2004.

[17] H. Nikkhajoei and R. Lasseter, "Distributed generation interface to the certs microgrid," *Power Delivery, IEEE Transactions on*, vol. 24, pp. 1598–1608, July 2009.

[18] A. Tuladhar, H. Jin, T. Unger, and K. Mauch, "Parallel operation of single phase inverter modules with no control interconnections," in *Applied Power Electronics Conference and Exposition, 1997. APEC '97 Conference Proceedings 1997., Twelfth Annual*, vol. 1, pp. 94–100 vol.1, Feb 1997.

[19] K. Strunz, R. Fletcher, R. Campbell, and F. Gao, "Developing benchmark models for low-voltage distribution feeders," in *Power & Energy Society General Meeting, 2009. PES '09. IEEE*, pp. 1–3, July 2009.

[20] L. D. Bailey, "Canadian distribution network system: Research and applica-

tions," in *3rd International Conference on Integration of Renewable and Distributed Energy Resources, Nice, France*, Dec. 2008.

[21] K. S. S. Papathanassiou, N. Hatziargyriou, "A benchmark low voltage microgrid network," in *CIGRE Symposium, Athens, 13-16*, April 2005.

[22] Z. S. K. Strunz, S. Barsali, "Cigre task force c6.04.02: Developing benchmark models for integrating distributed energy resources," tech. rep., CIGRE Study Committee C6 Colloquium, Cape Town, South Africa, 24 Oct. 2005.

[23] F. Peng, Y. W. Li, and L. Tolbert, "Control and protection of power electronics interfaced distributed generation systems in a customer-driven microgrid," in *Power & Energy Society General Meeting, 2009. PES '09. IEEE*, pp. 1–8, July 2009.

[24] M. Dai, M. Marwali, J.-W. Jung, and A. Keyhani, "Power flow control of a single distributed generation unit with nonlinear local load," in *Power Systems Conference and Exposition, 2004. IEEE PES*, pp. 398–403 vol.1, Oct. 2004.

[25] H. Zeineldin, E. El-Saadany, and M. Salama, "Distributed generation microgrid operation: Control and protection," in *Power Systems Conference: Advanced Metering, Protection, Control, Communication, and Distributed Resources, 2006. PS '06*, pp. 105–111, March 2006.

[26] N. Pogaku, M. Prodanovic, and T. Green, "Modeling, analysis and testing of autonomous operation of an inverter-based microgrid," *Power Electronics, IEEE Transactions on*, vol. 22, pp. 613–625, March 2007.

[27] A. F. A. Oudalov, "Adaptive network protection in microgrids." Available: http://www.microgrids.eu/documents/519.pdf.

[28] M. Chandorkar, D. Divan, and R. Adapa, "Control of parallel connected inverters in standalone ac supply systems," *Industry Applications, IEEE Transactions on*, vol. 29, pp. 136–143, Jan/Feb 1993.

[29] A. Engler and N. Soultanis, "Droop control in lv-grids," in *Future Power Systems, 2005 International Conference on*, pp. 6 pp.–6, Nov. 2005.

[30] Y. W. Li, "Control and resonance damping of voltage source and current source converters with lc filters," *Industrial Electronics, IEEE Transactions on*, vol. 56, pp. 1511–1521, May 2009.

[31] Y. W. Li, D. Vilathgamuwa, and P. C. Loh, "Microgrid power quality enhancement using a three-phase four-wire grid-interfacing compensator," *Industry Applications, IEEE Transactions on*, vol. 41, pp. 1707–1719, Nov.-Dec. 2005.

[32] Y. W. Li, F. Blaabjerg, D. Vilathgamuwa, and P. C. Loh, "Design and comparison of high performance stationary-frame controllers for dvr implementation," *Power Electronics, IEEE Transactions on*, vol. 22, pp. 602–612, March 2007.

[33] D. Zmood, D. Holmes, and G. Bode, "Frequency domain analysis of three phase linear current regulators," in *Industry Applications Conference, 1999. Thirty-Fourth IAS Annual Meeting. Conference Record of the 1999 IEEE*, vol. 2, pp. 818–825 vol.2, 1999.

[34] D. Zmood and D. Holmes, "Stationary frame current regulation of pwm inverters

with zero steady state error," in *Power Electronics Specialists Conference, 1999. PESC 99. 30th Annual IEEE*, vol. 2, pp. 1185–1190 vol.2, 1999.

[35] Y. W. Li, D. Vilathgamuwa, and P. C. Loh, "Robust control scheme for a microgrid with pfc capacitor connected," *Industry Applications, IEEE Transactions on*, vol. 43, pp. 1172–1182, Sept.-oct. 2007.

[36] F. Katiraei and M. Iravani, "Power management strategies for a microgrid with multiple distributed generation units," *Power Systems, IEEE Transactions on*, vol. 21, pp. 1821–1831, Nov. 2006.

[37] J. Guerrero, L. GarciadeVicuna, J. Matas, M. Castilla, and J. Miret, "Output impedance design of parallel-connected ups inverters with wireless load-sharing control," *Industrial Electronics, IEEE Transactions on*, vol. 52, pp. 1126–1135, Aug. 2005.

[38] M. Marwali, J.-W. Jung, and A. Keyhani, "Control of distributed generation systems - part ii: Load sharing control," *Power Electronics, IEEE Transactions on*, vol. 19, pp. 1551–1561, Nov. 2004.

[39] J. Guerrero, J. Matas, L. G. de Vicuna, M. Castilla, and J. Miret, "Decentralized control for parallel operation of distributed generation inverters using resistive output impedance," *Industrial Electronics, IEEE Transactions on*, vol. 54, pp. 994–1004, April 2007.

[40] P. Kundur, *Power system stability and control.* McGraw-Hill, Inc, 1994.

[41] Y. Mohamed and E. El-Saadany, "Adaptive decentralized droop controller to preserve power sharing stability of paralleled inverters in distributed generation

microgrids," *Power Electronics, IEEE Transactions on*, vol. 23, pp. 2806–2816, Nov. 2008.

[42] E. Coelho, P. Cortizo, and P. Garcia, "Small signal stability for single phase inverter connected to stiff ac system," in *Industry Applications Conference, 1999. Thirty-Fourth IAS Annual Meeting. Conference Record of the 1999 IEEE*, vol. 4, pp. 2180–2187 vol.4, 1999.

[43] E. Coelho, P. Cortizo, and P. Garcia, "Small-signal stability for parallel-connected inverters in stand-alone ac supply systems," *Industry Applications, IEEE Transactions on*, vol. 38, pp. 533–542, Mar/Apr 2002.

[44] E. Barklund, N. Pogaku, M. Prodanovic, C. Hernandez-Aramburo, and T. Green, "Energy management in autonomous microgrid using stability-constrained droop control of inverters," *Power Electronics, IEEE Transactions on*, vol. 23, pp. 2346–2352, Sept. 2008.

[45] J. Guerrero, L. de Vicuna, J. Matas, M. Castilla, and J. Miret, "A wireless controller to enhance dynamic performance of parallel inverters in distributed generation systems," *Power Electronics, IEEE Transactions on*, vol. 19, pp. 1205–1213, Sept. 2004.

[46] K. De Brabandere, B. Bolsens, J. Van den Keybus, A. Woyte, J. Driesen, and R. Belmans, "A voltage and frequency droop control method for parallel inverters," *Power Electronics, IEEE Transactions on*, vol. 22, pp. 1107–1115, July 2007.

[47] C.-T. Lee, C.-C. Chuang, C.-C. Chu, and P.-T. Cheng, "Control strategies for

distributed energy resources interface converters in the low voltage microgrid," in *Energy Conversion Congress and Exposition, 2009. ECCE. IEEE*, pp. 2022–2029, Sept. 2009.

[48] "Certs microgrid concept." available: http://certs.lbl.gov/certs-der-micro.html.